# A discontinuous Galerkin method for two-phase flow in a porous medium enforcing $H(\mathrm{div})$ velocity and continuous capillary pressure

**Todd Arbogast · Mika Juntunen · Jamie Pool · Mary F. Wheeler**

**Abstract** We consider the slightly compressible, two-phase flow problem in a porous medium with capillary pressure. The problem is solved using the implicit pressure, explicit saturation method (IMPES), and the convergence is accelerated with iterative coupling of the equations. We use discontinuous Galerkin to discretize both the pressure and saturation equations. We apply two improvements, which are projecting the flux to the mass conservative $H(\mathrm{div})$-space and penalizing the jump in capillary pressure in the saturation equation. We also discuss the need and use of slope limiters, and the choice of primary variables in discretization. The methods are verified with two and three dimensional numerical examples. The results show that the modifications stabilize the method and improve the solution.

Todd Arbogast · Jamie Pool · Mary F. Wheeler
The University of Texas at Austin, Institute for Computational Engineering and Sciences, 201 East 24th St. Stop C0200, Austin, TX 78712, USA
E-mail: arbogast@ices.utexas.edu, jpool@math.utexas.edu, mfw@ices.utexas.edu

Mika Juntunen
Aalto University School of Science, Department of Mathematics and Systems Analysis, P.O. Box 11000, 00076 Aalto, Finland
E-mail: mojuntun@gmail.com

# 1 Introduction

We consider the problem of slightly compressible two-phase flow in a porous medium, which is the simplest equation for subsurface flow in reservoir modeling. Solving this problem effectively and accurately is requisite for solving the more elaborate models of, e.g., $CO_2$ sequestration or enhanced oil recovery [6]. We assume that each phase has its own pressure, so there is capillary pressure between the phases. Taking this effect into account is essential for the validity of the model in subsurface applications [12]. We describe our problem in more detail in Section 2.1.

In this article we solve the system using the implicit pressure, explicit saturation method (IMPES) [5]. In this approach the problem is decoupled to pressure and saturation equations, and then solved sequentially. To reduce the error of decoupling, we use iterative coupling to solve the pair of decoupled equations. The effectiveness of this iterative coupling was demonstrated in, e.g., [7, 15, 14, 13]. We recall the IMPES algorithm in Section 2.2, using the splitting advocated by Hoteit and Firoozabadi [12]. We also discuss choosing the reference pressure for the problem when capillary pressure is present.

We choose to discretize the equations using discontinuous Galerkin (DG) for both of the decoupled equations. This DG-DG-method is briefly described in Section 3, see, e.g., [14, 8] for a more detailed derivation. Another popular method is to solve the pressure equation using mixed finite elements (MFE), and use DG only for the saturation equation. For more details on the MFE-DG-method, see, e.g., [17, 1]. In Section 3.2 we show how the flux coming from the DG-DG approach can be post processed into a locally mass conservative $H(\mathrm{div})$-space flux, imitating the MFE-DG approach. This post processing stabilizes the saturation part of the problem in our DG-DG approach. The same idea is applied also in [2, 9, 11, 10].

In Section 3.3, we discuss a technique for maintaining the continuity of capillary pressure. In [9] this modification is applied to a global pressure formulation. The idea is to introduce a penalty for the jump in capillary pressure in the saturation equation. In the case of only one capillary pressure curve throughout the domain, this forces the saturation to be continuous, which is physically correct. In the case of multiple capillary pressure curves, this improvement allows the saturation to jump at the interface between distinct capillary pressure curves, and instead enforces the physically relevant continuity of capillary pressure. This method is able to capture the discontinuity of saturation even when the absolute difference in capillary pressures is small.

By using several test examples, we demonstrate the numerical performance of our method. Two dimensional examples are given in Section 4 to illustrate the ideas in a simple setting. More interesting three dimensional examples with gravity and realistic Brooks-Corey and Van Genuchten capillary pressure functions are given in Section 5. The examples are computed with a research code developed at the Center for Subsurface Modeling [16] of the University of Texas at Austin.

Finally, a section summarizing our conclusions and giving further discussion ends the paper.

## 2 Problem formulation

In this section we recall the two-phase Darcy problem modeling subsurface flow and the IMPES algorithm used for solving the non-linear equations. The presentation is brief; for more details see, e.g., [5].

### 2.1 The continuous problem

Our model problem is for slightly compressible two-phase flow. The mass conservation equation states that

$$\frac{\partial \phi \rho_i S_i}{\partial t} + \nabla \cdot \mathbf{u}_i = f_i, \quad i = w, n, \tag{1}$$

in which $\phi$ is the porosity, $\rho_i$ is the density, $S_i$ is the saturation, $\mathbf{u}_i$ is the flux, $f_i$ is the source/sink, and subscripts $w$ and $n$ stand for the wetting and non-wetting phases respectively. Darcy's law gives

$$\mathbf{u}_i = \frac{-k_i K \rho_i}{\mu_i} (\nabla p_i - \rho_i g \nabla D), \tag{2}$$

in which $k_i$ is the relative permeability, $K$ is the absolute permeability, $\mu_i$ is the viscosity, $p_i$ is the pressure, $g$ is the gravity, and $\nabla D$ defines the direction of gravity (being the gradient of depth $D$). The equations are coupled nonlinearly

through relative permeability, capillary pressure, and density. Relative permeability is a known function of saturation

$$k_i = k_i(S_w). \tag{3}$$

The capillary pressure function models the pressure difference between the wetting and non-wetting phases. It is also a known function of saturation

$$p_c = p_n - p_w = p_c(S_w). \tag{4}$$

We assume slight compressibility [3,13], so

$$\rho_i = \rho_i(p_i) = \rho_{\mathrm{ref},i} e^{c_i p_i}, \tag{5}$$

in which $c_i$ is the known compressibility coefficient and $\rho_{\mathrm{ref},i}$ is the reference density at the reference pressure $p_{\mathrm{ref},i} = 0$.

The model assumes that all the pores are filled with fluid,

$$S_w + S_n = 1, \tag{6}$$

and in what follows, we assume that porosity $\phi$ and viscosity $\mu_i$ are constants for simplicity of exposition.

### 2.2 The IMPES algorithm with iterative coupling

The IMPES algorithm decouples the equations and solves them sequentially. For completeness we present the IMPES equations below. The first step is to sum the mass conservation equations (1) for both phases

$$\nabla \cdot (\mathbf{u_w} + \mathbf{u}_n) = f_w + f_n - \phi \left( \frac{\partial \rho_w S_w}{\partial t} + \frac{\partial \rho_n S_n}{\partial t} \right). \tag{7}$$

In practice, the mass conservation equations (1) are scaled with the reference density $\rho_{\mathrm{ref},i}$. If we suppose for the moment that the densities were constant, equation (6) shows that the last term above disappears, i.e.,

$$\frac{\partial \rho_w S_w}{\partial t} + \frac{\partial \rho_n S_n}{\partial t} = 0, \tag{8}$$

and hence

$$\nabla \cdot (\mathbf{u_w} + \mathbf{u}_n) = f_w + f_n. \tag{9}$$

With the slight compressibility assumption, the last term in (7) is indeed very small and is often neglected. For simplicity, we will assume in the derivation that this term vanishes. However, we emphasize that in our numerical examples, this term is present.

Next we modify (9) by using Darcy's law (2) and the definition of capillary pressure (4) to obtain

$$-\nabla \cdot (\lambda_t K \nabla p_w + \lambda_n K \nabla p_c - (\rho \lambda)_t g K \nabla D) = f_t \tag{10}$$

in which $\lambda_i = k_i \rho_i / \mu_i$, $\lambda_t = \lambda_w + \lambda_n$, $(\rho \lambda)_t = \rho_w \lambda_w + \rho_n \lambda_n$, and $f_t = f_w + f_n$. The subscript $t$ stands for total. Above we have chosen the wetting phase pressure $p_w$ to be the primary

variable. We will discuss the choice of reference pressure in more detail at the end of this section.

Assume we know the solution of the pressure and saturation at time $t^k$, that is, we know $p_w^k$ and $S_w^k$. To compute the pressure $p_w^{k+1}$ at time $t^{k+1}$ we time lag the saturation to compute $\lambda_i^k$ and $p_c^k$, and time lag pressure to get density $\rho_i^k$. Rearranging the terms gives

$$-\nabla \cdot (\lambda_t^k K \nabla p_w^{k+1}) = f_t + \nabla \cdot (\lambda_n^k K \nabla p_c^k - (\rho \lambda)_t^k g K \nabla D), \quad (11)$$

in which the unknown $p_w^{k+1}$ is on the left and the right hand side is known. This is the equation for the implicit pressure step of the IMPES algorithm, although we will modify it to the form (13) later.

Once we have the wetting phase pressure at time $t^{k+1}$, we solve for the say, wetting phase saturation at time $t^{k+1}$ using an explicit time stepping in the mass conservation equation (1)

$$\frac{\phi \rho_w^{k+1} S_w^{k+1}}{\Delta t} = f_w - \nabla \cdot \mathbf{u}_w^{k+1} + \frac{\phi \rho_w^k S_w^k}{\Delta t}, \quad (12)$$

in which $\Delta t = t^{k+1} - t^k$ and the velocity $\mathbf{u}_w^{k+1}$ is computed using Darcy's law (2), again time lagging the saturation but using $p_w^{k+1}$, so that (12) is an explicit equation for $S_w^{k+1}$. How to compute the velocity properly is discussed in more detail in Section 3.2. The previous equation (12) is the explicit saturation step of the IMPES algorithm.

## 2.3 Enhancing the IMPES algorithm

In this section we discuss enhancements to the IMPES algorithm to make it more effective in practice. The enhancements are taking shorter saturation steps, iterative coupling, and choosing the reference pressure.

*Shorter saturation steps.* In reservoir simulation it is often the case that the saturation part of the IMPES algorithm has much more rapid changes than the pressure part. In fact, the pressure is almost independent of time if the wells are operated with constant pressure or constant flow. Therefore it is well-known to be useful to take shorter time steps in the saturation equation. For example, if the time step in the pressure equation is $\Delta t$, one can take $N$ saturation time steps of length $\Delta t / N$ before taking a new pressure step. In the intermediate steps, the pressure is interpolated linearly. Taking several saturation steps can speed up the simulation considerably since the saturation equation is explicit, which is much easier to solve than the implicit pressure equation. The step size of the saturation equation should be determined according to the CFL condition. This could be done automatically but in this work we have predefined the number of saturation steps. In the numerical examples presented in this paper we have used roughly 10 saturation steps for each

pressure step. This has been a favorable ratio in terms of how long it takes to run the simulation.

*Iterative coupling.* The IMPES algorithm decouples the non-linear equations and solves them sequentially; hence, the results are sometimes inaccurate. There may be a loss of mass balance and a mismatch in the acquired pressure and saturation. If either of these is detected a simple improvement is to iterate by redoing the time step using the new pressure and saturation in equation (11). The pseudo code for one complete time step of this algorithm follows.

0. Set the iteration index $\ell = 0$, $p_w^{k,0} = p_w^k$, and $S_w^{k,0} = S_w^k$.
1. Given $p_w^{k,\ell}$ and $S_w^{k,\ell}$, solve for $p_w^{k,\ell+1}$ using (11), i.e.,

$$-\nabla \cdot (\lambda_t^{k,\ell} K \nabla p_w^{k,\ell+1})$$
$$= f_t + \nabla \cdot (\lambda_n^{k,\ell} K \nabla p_c^{k,\ell} - (\rho \lambda)_t^{k,\ell} g K \nabla D).$$

2. Given $p_w^{k,\ell+1}$ and $S_w^{k,\ell}$, solve for $S_w^{k,\ell+1}$ using $N$ steps of (12). That is, for parameter $m = 0, 1, 2, \ldots, N$, we interpolate the pressure as

$$p_w^{k,\ell,m} = p_w^k + \frac{m}{N}(p_w^{k,\ell+1} - p_w^k),$$

we set $S_w^{k,\ell,0} = S_w^{k,\ell}$, and, for $m = 0, 1, \ldots, N-1$, we solve for $S^{k,\ell,m+1}$ from

$$\frac{\phi \rho_w^{k,\ell,m+1} S_w^{k,\ell,m+1}}{\Delta t / N} = f_w - \nabla \cdot \mathbf{u}_w^{k,\ell,m+1} + \frac{\phi \rho_w^{k,\ell,m} S_w^{k,\ell,m}}{\Delta t / N}.$$

Finally, $S_w^{k,\ell+1} = S_w^{k,\ell,N}$.
3. Check for convergence. If converged, set $p_w^{k+1} = p_w^{k,\ell+1}$ and $S_w^{k+1} = S_w^{k,\ell+1}$ and continue to the next time step; otherwise, advance $\ell \hookrightarrow \ell + 1$ and go to step 1.

In the numerical examples presented in this article, we always use this iterative coupling technique.

*Choosing the reference pressure.* In the IMPES algorithm described above we have used the wetting phase pressure and saturation as the reference variables. If one chooses the non-wetting phase variables as the reference, the pressure equation (11) becomes

$$-\nabla \cdot (\lambda_t^k K \nabla p_n^{k+1})$$
$$= f_t + \nabla \cdot (-\lambda_w^k K \nabla p_c^k - (\rho \lambda)_t^k g K \nabla D). \quad (13)$$

The difference between equations (11) and (13) is in the capillary pressure term, involving $\lambda_n^k \nabla p_c^k$ for the wetting phase and $-\lambda_w^k \nabla p_c^k$ for the non-wetting phase reference pressure.

If only one of the phases is present, it is natural to use the existing phase as the reference variable. However, numerically the choice of reference variables becomes important already near the residual saturations. For example, suppose the saturation is near the wetting phase residual saturation $S_{w,r}$. Then the non-wetting phase relative permeability reaches its highest value, $k_n(S_{w,r}) \sim 1$, and at the same time

the capillary pressure tends to infinity, $p_c(S_{w,r}) \to \infty$. Thus the term $\lambda_n^k \nabla p_c^k$, needed when using the wetting phase pressure as reference, tends to infinity. However, near the wetting phase residual saturation, the wetting phase relative permeability vanishes, $k_w(S_{w,r}) = 0$. Hence the term $-\lambda_w^k \nabla p_c^k$, needed when using the non-wetting phase as reference pressure, stays bounded.

Observe that the same problem will also appear for the non-wetting phase reference pressure if the derivative of the capillary pressure tends to infinity at the non-wetting phase residual saturation, e.g., in a Van Genuchten model. We will study the effect of reference pressure with numerical examples in Sections 4 and 5.

## 3 Discretization

### 3.1 DG-DG two-phase flow

We present the discrete form of the problem (1)–(6) in this section, in the form of (11) and (12) using the discontinuous Galerkin, (DG), method. For a more detailed derivation of DG methods for flows in porous media see, e.g., [14,8] and the citations therein.

Assume we are solving the problem in the domain $\Omega$ that has piecewise smooth boundary $\partial\Omega$. For simplicity, we assume the boundary is divided into three non-overlapping pieces: $\Gamma_{\text{in}}$ denotes the inflow boundary where both pressure $p_w^{\text{in}}$ and saturation $S_w^{\text{in}}$ are defined, $\Gamma_{\text{out}}$ denotes the outflow boundary where only pressure $p_w^{\text{out}}$ needs to be given, and $\Gamma_0$ denotes the no-flow boundary where the total normal flow is zero.

We assume the domain $\Omega$ is divided into a set of non-overlapping elements $E$, and the collection of elements, the mesh, is denoted by $\mathscr{T}_h$, where $h$ denotes the maximum diameter of the elements. We assume that the mesh is quasi-uniform, i.e., the mesh diameter is bounded from below. We denote by $\mathscr{G}_h$ the collection of edges (in 2 dimensions) or faces (in 3 dimensions) of the mesh $\mathscr{T}_h$. The subset $\mathscr{G}_h^{\text{int}}$ denotes the internal edges, and the subsets $\mathscr{G}_h^{\text{in}}$, $\mathscr{G}_h^{\text{out}}$, and $\mathscr{G}_h^0$ denote the inflow, outflow and no-flow boundary edges, respectively.

The approximation spaces for the solution are

$$\mathscr{W}^l = \{q \in L^2(\Omega) : q|_E \in \mathscr{P}^l(E), \forall E \in \mathscr{T}_h\}, \tag{14}$$

meaning that we use piecewise polynomials of order $l$ and the space is discontinuous between elements. In the numerical examples, we use space $\mathscr{W}^1$ for pressure and either $\mathscr{W}^0$ or $\mathscr{W}^1$ for the saturation.

On an edge $e \subset \partial\Omega$, let $\nu$ be the outer normal to $\Omega$. On an edge $e$ between elements $E_1$ and $E_2$, let $\nu$ be the outer normal of element $E_1$ and define $q_i$ as the trace of $q|_{E_i}$ on $e$. Then $\{\{q\}\} = (q_1 + q_2)/2$ denotes the average and $[\![q]\!] = q_1 - q_2$ denotes the jump.

Now we are ready to form the weak form of the pressure step (11). Find $p_w^{k+1} \in \mathscr{W}^l$, $l \geq 1$, such that

$$\sum_{E \in \mathscr{T}_h} \left(\lambda_t^k K \nabla p_w^{k+1}, \nabla q\right)_E$$
$$+ \sum_{e \in \mathscr{G}_h^{\text{int}}} \Big\{ -\langle \{\{\lambda_t^k K \nabla p_w^{k+1} \cdot \nu\}\}, [\![q]\!] \rangle_e$$
$$- \theta \langle \{\{\lambda_t^k K \nabla q \cdot \nu\}\}, [\![p_w^{k+1}]\!] \rangle_e$$
$$+ \frac{\gamma}{h_e} \langle [\![p_w^{k+1}]\!], [\![q]\!] \rangle_e \Big\}$$
$$+ \sum_{e \in \mathscr{G}_h^{\text{in}} \cup \mathscr{G}_h^{\text{out}}} \Big\{ -\langle \lambda_t^k K \nabla p_w^{k+1} \cdot \nu, q \rangle_e$$
$$- \theta \langle \lambda_t^k K \nabla q \cdot \nu, p_w^{k+1} \rangle_e + \frac{\gamma}{h_e} \langle p_w^{k+1}, q \rangle_e \Big\}$$
$$= \sum_{E \in \mathscr{T}_h} \Big\{ (f_t, q)_E - \left(\lambda_n^k K \nabla p_c^k - (\rho\lambda)_t^k g K \nabla D, \nabla q\right)_E \Big\}$$
$$+ \sum_{e \in \mathscr{G}_h^{\text{int}}} \langle \{\{(\lambda_n^k K \nabla p_c^k - (\rho\lambda)_t^k g K \nabla D) \cdot \nu\}\}, [\![q]\!] \rangle_e$$
$$+ \sum_{e \in \mathscr{G}_h^{\text{in}} \cup \mathscr{G}_h^{\text{out}}} \langle (\lambda_n^k K \nabla p_c^k - (\rho\lambda)_t^k g K \nabla D) \cdot \nu, q \rangle_e$$
$$+ \sum_{e \in \mathscr{G}_h^{\text{in}}} \Big\{ -\theta \langle \lambda_t^k K \nabla q \cdot \nu, p_w^{\text{in}} \rangle_e + \frac{\gamma}{h_e} \langle p_w^{\text{in}}, q \rangle_e \Big\}$$
$$+ \sum_{e \in \mathscr{G}_h^{\text{out}}} \Big\{ -\theta \langle \lambda_t^k K \nabla q \cdot \nu, p_w^{\text{out}} \rangle_e + \frac{\gamma}{h_e} \langle p_w^{\text{out}}, q \rangle_e \Big\} \tag{15}$$

for all $q \in \mathscr{W}^l$, where $\gamma > 0$ is the stability parameter and $\theta = -1, 0, 1$ defines the method. The three values of $\theta$ correspond to NIPG, IIPG, and SIPG[1], respectively. We remark that $\gamma$ should probably be scaled by the magnitude of the permeability. For example, one could scale $\gamma$ by some average of the total mobility times the permeability in the normal direction, $\lambda_t K_\nu = \lambda_t \nu^T K \nu$. However, this was not required in the numerical examples we discuss in Sections 4–5.

Formally, the weak form for the saturation step (12) is: Find $S_w^{k+1} \in \mathscr{W}^m$, $m \geq 0$, such that

$$\sum_{E \in \mathscr{T}_h} \left(\frac{\phi \rho_w^{k+1} S_w^{k+1}}{\Delta t}, z\right)_E$$
$$= \sum_{E \in \mathscr{T}_h} \Big\{ \left(\frac{\phi \rho_w^k S_w^k}{\Delta t}, z\right)_E + (f_w, z)_E - \left(\nabla \cdot \mathbf{u}_w^{k+1}, z\right)_E \Big\} \tag{16}$$

for all $z \in \mathscr{W}^m$. Since we only solve for the wetting phase pressure, $p_w^{k+1}$, we do not directly have the wetting phase velocity $\mathbf{u}_w^{k+1}$. Instead, we need to construct the velocity using Darcy's law (2). To this end, we integrate by parts in the

---

[1] The acronyms stand for non-symmetric (N), incomplete (I), and symmetric (S) interior penalty Galerkin (IPG).

last term to obtain

$$\sum_{E\in\mathscr{T}_h}\left(\frac{\phi\rho_w^{k+1}S_w^{k+1}}{\Delta t},z\right)_E$$
$$=\sum_{E\in\mathscr{T}_h}\left\{\left(\frac{\phi\rho_w^k S_w^k}{\Delta t},z\right)_E+\left(f_w,z\right)_E+\left(\mathbf{u}_w^{k+1},\nabla z\right)_E\right\}$$
$$-\sum_{e\in\mathscr{G}_h^{\mathrm{int}}\cup\mathscr{G}_h^{\mathrm{in}}\cup\mathscr{G}_h^{\mathrm{out}}}\langle\mathbf{u}_w^{k+1}\cdot\mathbf{v},[\![z]\!]\rangle_e. \tag{17}$$

Inside the elements we can use Darcy's law, but on the edges $e$ we need to take into account the discontinuities, that is, the numerical flux. On internal edges, the flux is computed as

$$\mathbf{u}_w^{k+1}\cdot\mathbf{v}=(\lambda_w^k K)^{\mathrm{up}}\{\!\{(\nabla p_w^{k+1}-\rho_w^{k+1}g\nabla D)\cdot\mathbf{v}\}\!\}$$
$$+(\frac{\lambda_w}{\lambda_t})^{\mathrm{up}}\frac{\gamma}{h_e}[\![p_w^{k+1}]\!], \tag{18}$$

in which $(\cdot)^{\mathrm{up}}$ means that the quantities are up-winded. Up-winding means that on an edge $e$, the values are computed using the data of the outflow element. On in/outflow boundaries the flux is computed in similar manner; the difference is that we do not need to use the mean value, and that the jump is computed against the given boundary data. The last term in (18) corresponds to the numerical flux stemming from the discontinuity of the pressure approximation, see, e.g., [9] for more details.

Using (18), the saturation step (16) becomes

$$\sum_{E\in\mathscr{T}_h}\left(\frac{\phi\rho_w^{k+1}S_w^{k+1}}{\Delta t},z\right)_E$$
$$=\sum_{E\in\mathscr{T}_h}\Big\{\left(\frac{\phi\rho_w^k S_w^k}{\Delta t},z\right)_E+\left(f_w,z\right)_E$$
$$+((\lambda_w^k K)^{\mathrm{up}}(\nabla p_w^{k+1}-\rho_w^{k+1}g\nabla D),\nabla z)_E\Big\}$$
$$-\sum_{e\in\mathscr{G}_h^{\mathrm{int}}}\Big\langle(\lambda_w^k K)^{\mathrm{up}}\{\!\{(\nabla p_w^{k+1}-\rho_w^{k+1}g\nabla D)\cdot\mathbf{v}\}\!\}$$
$$+\left(\frac{\lambda_w}{\lambda_t}\right)^{\mathrm{up}}\frac{\gamma}{h_e}[\![p_w^{k+1}]\!],[\![z]\!]\Big\rangle_e$$
$$-\sum_{e\in\mathscr{G}_h^{\mathrm{in}}}\Big\langle(\lambda_w^k K)^{\mathrm{up}}(\nabla p_w^{k+1}-\rho_w^{k+1}g\nabla D)\cdot\mathbf{v}$$
$$+\left(\frac{\lambda_w}{\lambda_t}\right)^{\mathrm{up}}\frac{\gamma}{h_e}(p_w^{k+1}-p_w^{\mathrm{in}}),z\Big\rangle_e$$
$$-\sum_{e\in\mathscr{G}_h^{\mathrm{out}}}\Big\langle(\lambda_w^k K)^{\mathrm{up}}(\nabla p_w^{k+1}-\rho_w^{k+1}g\nabla D)\cdot\mathbf{v}$$
$$+\left(\frac{\lambda_w}{\lambda_t}\right)^{\mathrm{up}}\frac{\gamma}{h_e}(p_w^{k+1}-p_w^{\mathrm{out}}),z\Big\rangle_e. \tag{19}$$

The basic overall discrete system is given by (15) and (19). Below we discuss two important modifications.

## 3.2 Projection to $H$(div)-space

In this section we show an alternative way of handling the flux needed in the pressure step (16) when $l=1$. The idea is to project the flux into the $H(\mathrm{div},\Omega)$-space, cf., [2,9,11, 10]. In practice, we project the flux onto the space defined by the lowest order Raviart-Thomas elements $(RT_0)$. For more details on mixed elements see, e.g., [4].

We seek to approximate the flux in the space spanned by $RT_0$-elements

$$\mathscr{V}=\{\mathbf{v}\in H(\mathrm{div},\Omega):v|_E\in RT_0(E),\forall E\in\mathscr{T}_h\}. \tag{20}$$

Using the divergence theorem,

$$(\nabla\cdot\mathbf{v},1)_E=\langle\mathbf{v}\cdot\mathbf{v},1\rangle_{\partial E} \tag{21}$$

and the fact that for $RT_0$ elements the divergence inside the elements is constant, as are the normal fluxes over each edge, gives

$$\nabla\cdot\widetilde{\mathbf{u}}|_E=\frac{1}{|E|}\langle\widetilde{\mathbf{u}}\cdot\mathbf{v},1\rangle_{\partial E} \tag{22}$$

for all $\widetilde{\mathbf{u}}\in\mathscr{V}$. Using equation (18) we get

$$\nabla\cdot\widetilde{\mathbf{u}}_w^{k+1}|_E=\frac{1}{|E|}\Big\langle(\lambda_w^k K)^{\mathrm{up}}\{\!\{(\nabla p_w^{k+1}-\rho_w^{k+1}g\nabla D)\cdot\mathbf{v}\}\!\}$$
$$+\left(\frac{\lambda_w}{\lambda_t}\right)^{\mathrm{up}}\frac{\gamma}{h_e}[\![p_w^{k+1}]\!],1\Big\rangle_{\partial E}. \tag{23}$$

For edges on the no-flow boundary, the integral is zero. For edges on either the inflow or outflow boundaries, we do not use the mean value, and the jump is against the given boundary data, similar to equation (19). After this local, intermediate step between the pressure and saturation steps, we now have divergence of the wetting phase flux in each element. Therefore, the saturation step becomes: When $l=1$, find $S_w^{k+1}\in\mathscr{W}^m,m>0$, such that

$$\sum_{E\in\mathscr{T}_h}\left(\frac{\phi\rho_w^{k+1}S_w^{k+1}}{\Delta t},z\right)_E$$
$$=\sum_{E\in\mathscr{T}_h}\Big\{(\frac{\phi\rho_w^k S_w^k}{\Delta t},z)_E+\left(f_w,z\right)_E-\left(\nabla\cdot\widetilde{\mathbf{u}}_w^{k+1},z\right)_E\Big\} \tag{24}$$

for all $z\in\mathscr{W}^m$. This is our alternative to (19).

*Remark 1* If we use piecewise constant saturations, $S_w\in\mathscr{W}^0$, we will naturally project the fluxes to $RT_0$. This is because on $E$ the test function $z=1$, and hence $\nabla z=0$ in equation (19), meaning that the alteration (24) is equivalent to the original formulation (19).

*Remark 2* Suppose the saturation $S_w^k$ is piecewise constant, and that the data is piecewise constant. Then using projected fluxes (24) will give piecewise constant $S_w^{k+1}$, even if $S_w\in\mathscr{W}^m,m\geq 1$. This is because the saturation step is, in this particular case, just an $L^2$-projection onto piecewise constants.

## 3.3 Penalty for discontinuity in capillary pressure

In the formulation above, the effect of capillary pressure appears explicitly only in the pressure step (15). In the saturation step, (19) or (24), the capillary effect appears implicitly through the flux that depends on the pressure. Hence we modify the saturation equation to take the capillary effect explicitly into account also in this step. Similar to [9], the idea is to add a penalty to discontinuity of the capillary pressure. The presented formulation assumes that the capillary pressure is continuous. The assumption may fail if the model has entry pressures and only one phase is present.

For simplicity we will work with saturation step (24) but the exact same procedure works for (19), as well. We propose to add to (24) the term

$$\sum_{e \in \mathscr{G}_h^{\text{int}}} -\frac{\sigma}{(1 + \{\{p_c^k\}\})\Delta t} \langle [\![p_c^{k+1}]\!], [\![z]\!] \rangle_e, \tag{25}$$

in which $\sigma > 0$ is a penalty parameter. Suppose the capillary pressure is a decreasing function of the wetting phase saturation. Then the negative sign corresponds to the sign convention chosen in equations (24) and (19). The scaling $1/(1 + \{\{p_c^k\}\})$ ensures that the penalty term is of the same scale as the rest of the terms. There is no need to scale with mesh size $h_e$, since using trace inequalities one can bound this term with the $H^1(\Omega)$-norm of the capillary pressure and the $L^2(\Omega)$-norm of the saturation, which correspond to the correct solution spaces. The factor 1 in the denominator is to prevent division by 0 when the capillary pressure is small.

Unfortunately, $p_c^k = p_c(S_w^k)$ is a non-linear function of saturation. To maintain computational efficiency, we will linearize this term. Using a linear approximation

$$\begin{aligned} p_c^{k+1} = p_c(S_w^{k+1}) &\approx p_c(S_w^k) + p_c'(S_w^k)(S_w^{k+1} - S_w^k) \\ &= p_c^k + p_c'^k(S_w^{k+1} - S_w^k), \end{aligned} \tag{26}$$

we get

$$\begin{aligned} &\sum_{e \in \mathscr{G}_h^{\text{int}}} -\frac{\sigma}{(1 + \{\{p_c^k\}\})\Delta t} \langle [\![p_c'^k S_w^{k+1}]\!], [\![z]\!] \rangle_e \\ &= \sum_{e \in \mathscr{G}_h^{\text{int}}} -\frac{\sigma}{(1 + \{\{p_c^k\}\})\Delta t} \langle [\![p_c'^k S_w^k - p_c^k]\!], [\![z]\!] \rangle_e, \end{aligned} \tag{27}$$

which is linear with respect to the unknown $S_w^{k+1}$. With this penalty for capillary pressure in place of (25), and using the

$H(\text{div}, \Omega)$-projection, the saturation step reads

$$\begin{aligned} &\sum_{E \in \mathscr{T}_h} \left( \frac{\phi \rho_w^{k+1} S_w^{k+1}}{\Delta t}, z \right)_E \\ &\quad - \sum_{e \in \mathscr{G}_h^{\text{int}}} \frac{\sigma}{(1 + \{\{p_c^k\}\})\Delta t} \langle [\![p_c'^k S_w^{k+1}]\!], [\![z]\!] \rangle_e \\ &= \sum_{E \in \mathscr{T}_h} \left\{ \left( \frac{\phi \rho_w^k S_w^k}{\Delta t}, z \right)_E + (f_w, z)_E - (\nabla \cdot \widetilde{\mathbf{u}}_w^{k+1}, z)_E \right\} \\ &\quad - \sum_{e \in \mathscr{G}_h^{\text{int}}} \frac{\sigma}{(1 + \{\{p_c^k\}\})\Delta t} \langle [\![p_c'^k S_w^k - p_c^k]\!], [\![z]\!] \rangle_e. \end{aligned} \tag{28}$$

*Remark 3* Suppose there is only one capillary pressure curve for the whole domain. If the curve is constant, the added terms will vanish, which is exactly what we want. If the curve is monotone, the added terms will enforce the continuity of saturation, which is the correct physical behavior for monotone capillary pressure.

To close this section, the overall discrete system is given by (15) and (28) with (23) when one uses the alternative $H(\text{div})$ velocity $\widetilde{\mathbf{u}}_w^{k+1}$, and otherwise by (15) and (19) plus (27). Iterative coupling as described in Section 2.3 can also be applied to the system.

## 4 Numerical examples in two dimensions

In this section we discuss numerical solutions to the slightly compressible two-phase flow problem in two space dimensions using the DG-DG discretization described in Section 3. Except where noted, we choose the pressure and saturation of the wetting phase, $P_w$ and $S_w$, as the primary variables.

The simulations are run for 600 days, starting with a time step of 0.001 days and which increases over time by the multiplier 1.2 to a maximum time step of 0.5 days. As mentioned earlier, it is useful to take shorter time steps in the saturation equation, so we take 10 saturation steps for every 1 pressure step. The computational domain is $(x, y) \in [0, 500] \times [0, 500]$ feet (and considered to be 100 feet thick). As shown in Fig. 1, the inflow boundary $\Gamma_{\text{in}}$ is $(x, y) \in \{0\} \times [400, 500]$, and the outflow boundary $\Gamma_{\text{out}}$ is $(x, y) \in \{500\} \times [0, 100]$. The rest of the boundary, $\Gamma_0$, is of no flow type. The initial pressure is set to 500 psi. The pressure boundary conditions on the inflow and outflow boundaries are 550 psi and 450 psi, respectively. The initial saturation is 0.2 and, in order to imitate a water flood, the inflow boundary condition is set to $S_w = 1$.

To make sure there is no instability coming from the pressure equation, we use the non-symmetric interior penalty Galerkin (NIPG) method ($\theta = -1$ in (15)). In all our numerical examples we use a piecewise linear basis, $l = 1$, to approximate the pressure. A pressure penalty of $\gamma = 10$ is used. Theoretically any penalty greater than 0 is acceptable
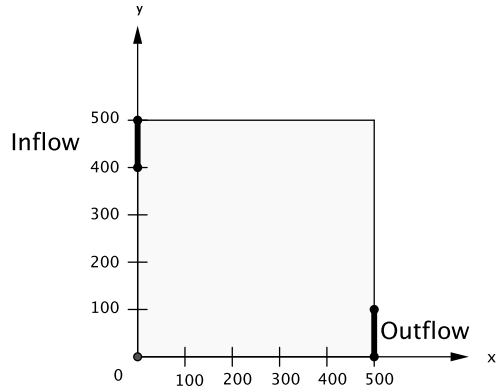
**Fig. 1** Computational domain as seen from above.



**Fig. 2** Validation example. The capillary pressure curve is on the top, and the relative permeability curves are on the bottom.

and numerical tests show that the solution is not sensitive to this parameter when it ranges from 5 to 50.

Except where noted, we use a linear approximation for the saturation, $m = 1$, and the penalty for the jump in capillary pressure uses $\sigma = 10$. The numerical solutions are not sensitive to this parameter when it is between 1 and 100. In addition, we use the projection to $H(\mathrm{div})$-space except where noted.

### 4.1 Validating the method

In this section we consider the problem where there is only one capillary pressure curve and take $K = 100$ millidarcy. The capillary pressure and relative permeability curves are similar to [12]. These capillary pressure curves are of the form $p_c(S_w) = -10\log(S_w)/\sqrt{K}$, i.e., inversely proportional to the permeability. Furthermore, the relative permeabilities are given as a function of the wetting phase saturation as $k_w = S_w^2$ and $k_n = (1 - S_w)^2$, see Fig. 2. The fluids are slightly compressible, with a water and oil compressibility of $10^{-12}$ and $10^{-10}$, respectively.

In order to determine the solution to the problem, we model the saturation with piecewise constant functions, $m = 0$, and view the solution on different size meshes. For these numerical tests the penalty for the discontinuity in capillary pressure (27) was not used. In addition, the projection to the $H(\mathrm{div})$-space (23) does not change the previous formulation (see Remark 1). The numerical results are shown in Fig. 3. Notice that as we refine the mesh, the solution remains the same. For these reasons we take these results to be a valid approximation of the solution that we can use as a baseline with which to compare further results. Henceforth we will not include the pressure curves, but we note that they are all consistent with those shown here.

Using piecewise linear functions to approximate the saturation, $m = 1$, we obtain the results in Fig. 4. These results include the penalty for discontinuous capillary pressure. There is some grid dependance on the coarser mesh,
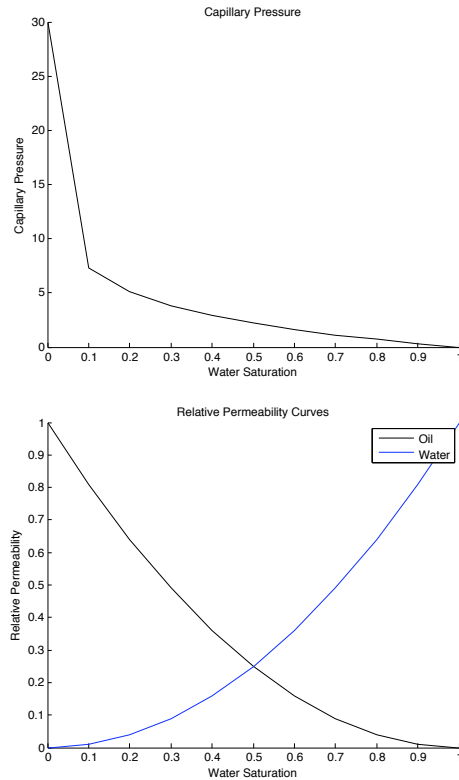
but this vanishes as the mesh is refined. The flux projection removes oscillations, so there is no need to use a local slope limiter. However, there are overshoots at the inflow, which increase over time. On the fine grid, the maximum value of the saturation is 1.163, which occurs at day 600. To handle this problem, we implemented a global slope limiter that enforces the saturation to stay between its maximum value 1 and minimum value 0. We use a limiter that guarantees that the saturation stays bounded without any tuning parameters. This limiter is discussed in [18]. We further note that the saturation plume travels the same distance using the piecewise linear basis functions as it did when we used the piecewise constants. This validates the proposed improvements, that is, the projection to $H(\mathrm{div})$ and adding a penalty for the jump in the capillary pressure.

We also computed the CFL time step limit for the validation runs. We report a typical case, the case of constant saturation (so without slope limiter) on the finest $15 \times 15$ grid using eight saturation steps per pressure step to the final time 600 days. The CFL time step at the beginning of the simulation is about 3 days. However, except for the first eight steps, the CFL time step is around 100 days throughout the simulation, ending at about 90 days. The actual saturation time step varies from about 0.00013 days initially to about 0.203 days by the end of the simulation, which is far below
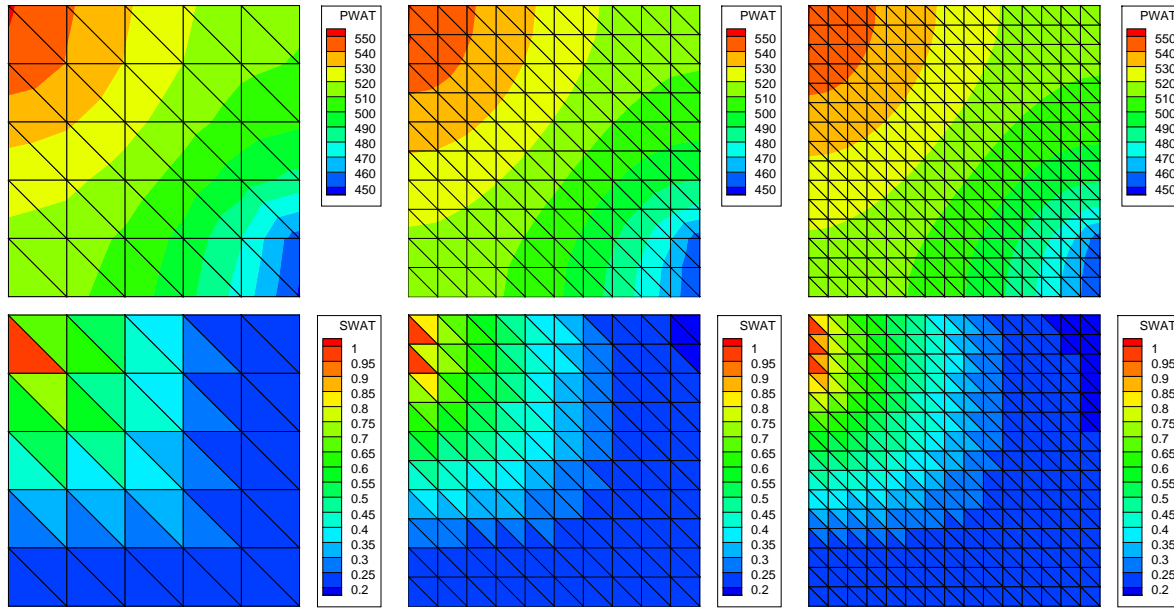
**Fig. 3** Validation Example. From right to left we use 50, 200, and 450 elements. Piecewise linear pressure solutions on the top. Piecewise constant saturation solutions on the bottom
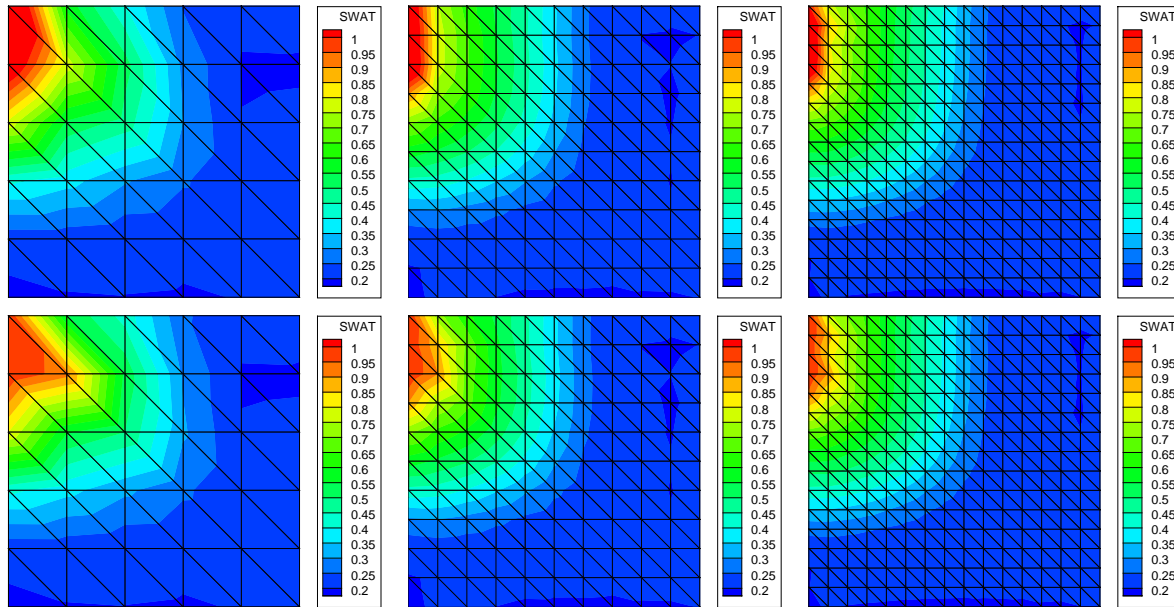


**Fig. 4** Validation example. Piecewise linear saturation solutions, on the top using no slope limiter, on the bottom using a global slope limiter.

the CFL limit. It could be increased, however, then the iterative coupling requires more iterations to achieve the mass balance. Since the saturation steps are explicit and cheap to compute, it is more effective in wall clock time to increase the number of saturation steps and reduce the number of iterative coupling iterations (which require solving the more expensive implicit pressure equation).

It was previously remarked (see Remark 2) that if at some time $t_k$ the saturation $S_w^k$ is piecewise constant, then using projected fluxes will give a piecewise constant solution $S_w^{k+1}$ at time $t_{k+1}$. We ran this case with linear saturations but no penalty to the discontinuity of capillary pressure. The saturation at 600 days is the same regardless if the test functions are piecewise linear or piecewise constant; both saturations appear the same as in Fig. 3. Observe also that here the projection to the $H(\mathrm{div})$ space removes the local oscillations from the (in principle) piecewise linear saturation.

## 4.2 Two Rock Types

In this section we look further at the improvements to the method by considering the case where there are two rock types. In the results in this section we are using the same computational domain as in the previous section, except now there is a second rock type located in the domain in the area $(x,y) \in [0,300] \times [200,300]$ feet, as shown in Fig. 5.
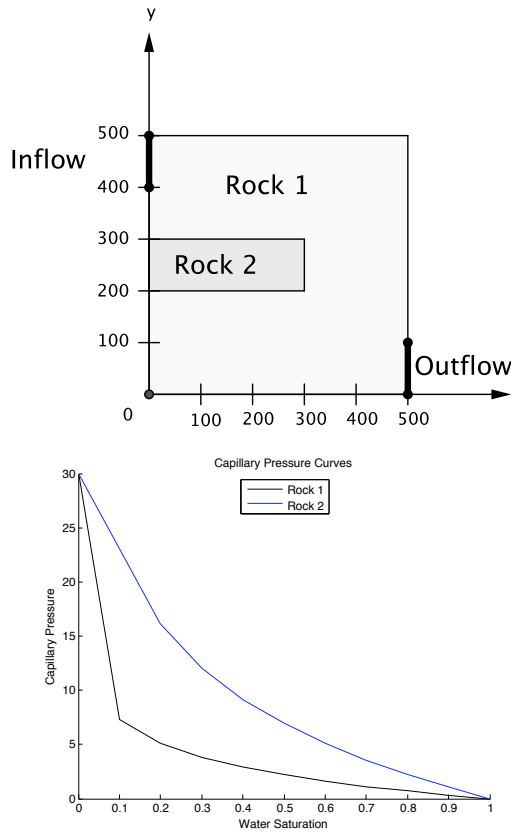


**Fig. 5** Two rock types in 2-D. Location of the two rocks in the computational domain and the associated capillary pressure curves.

The rocks will have different capillary pressure curves due to the difference in the permeabilities of the rocks. Rock Type 1 has a permeability of 100 millidarcy, and the second rock type has a permeability of 10 millidarcy. The capillary curves are shown in Fig. 5. The compressibility of water and oil is $10^{-7}$ and $10^{-5}$, respectively.

This time we take the initial condition for the saturation to be piecewise constant with a value of $S_w = 0.2$ in Rock Type 1, and in Rock Type 2 it is set to satisfy that the capillary pressure is continuous across the boundary.

We used the global slope limiter with these results and set the global maximum and minimum to be 1 and 0.2 respectively.

Shown in Fig. 6 are the saturation and pressure results at various times. We note that the pressure solution is smooth as we would expect. Looking at the saturation at the boundary of the rock types, we notice that the saturation is discontinuous, as expected. For example, the saturation is greater in Rock Type 2 so that it will respect the continuity of the capillary pressure that is explicitly required in the saturation step. We also see that because of the higher permeability in Rock 1, the saturation front moves faster around Rock 2 than going through it. By 1000 days the flow has come around the bend of the second rock type and is heading towards the outflow boundary.

## 4.3 Choosing the primary pressure

In this section we illustrate the problems that can occur with using the wetting phase as the primary pressure. We look at the same example of two rock types as before, except we change the initial condition so that the $S_w = 0$ everywhere, which is a valid choice with respect to the capillary pressure curves in Fig. 5. We also use the global slope limiter to enforce the global maximum and minimum value to be 1 and 0 respectively. When we do this, we get the results in Fig. 7. This simulation shows large oscillations in both the pressure and saturation solutions. The oscillations in the pressure are difficult to see, but they are the main source of oscillations to the saturation solution, which is evident in the figures. Observe that the oscillations are worse in Rock 1 where the capillary pressure has a steeper gradient near the residual saturation, which supports the discussion on choosing the reference pressure in Section 2.3.

We ran the problem with the same parameters but with the non-wetting phase as the primary pressure. Due to a computer code limitation, this changes our pressure boundary condition to be with respect to the non-wetting phase. Thus, this is not exactly the same problem as in the previous case, but it is very similar. We choose to look at times where the saturation front had reached approximately the same distance as in the previous case to compare the results, see Fig. 8. The speed of the front is different due to the obviously incorrect results obtained when using the water pressure. Observe that the speed of the front is similar to Fig. 6. The main improvement is of course that using the non-wetting phase pressure, we no longer have oscillations in the solution. The reason for the improvement is that we are avoiding the numerical instability problem discussed in Section 2.3.

## 4.4 Mesh refinement study

We next present a mesh refinement study in order to provide some quantification of the convergence of our method.
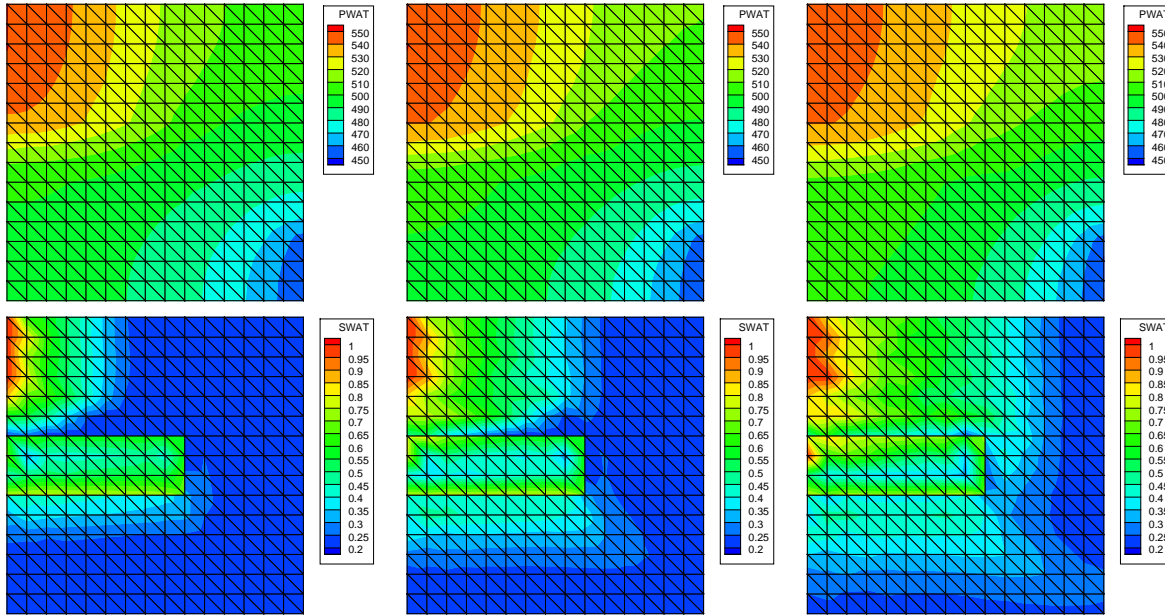
**Fig. 6** Two rock types in 2-D. Linear water pressure on the top, and saturation on the bottom. From left to right at day 300, 600, and 1000.
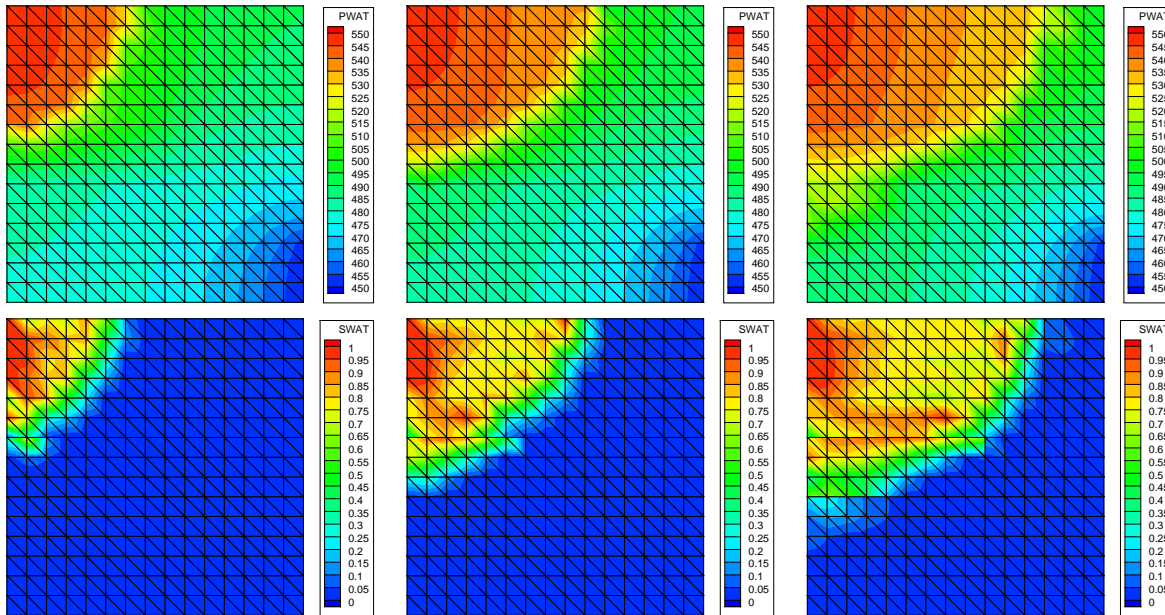


**Fig. 7** Primary pressure choice in 2-D. Water pressure (top) and water saturation (bottom) with initial saturation 0 and using water pressure as primary pressure. From left to right at day 500, 1000, and 1500.

Based on the discussion in Section 4.3, we use the non-wetting phase as the primary pressure. In order to make the problem run on a refined mesh with a short wall clock time, we made a few adjustments to the problem in Section 4.3. The computational domain is the area $[0,400] \times [0,400]$, with a second rock type located in the region $[0,200] \times [100,200]$. We also added several more points to the Capillary Pressure curves, as shown in Fig. 9.

This problem produced images comparable to those previously shown. We ran the problem on grids of size $8 \times 8$,

**Table 1** Mesh Refinement Study.

| Grid Size | Relative Pressure Error | Relative Saturation Error |
|-----------|------------------------|---------------------------|
| 8 | 0.00341 | 0.197 |
| 12 | 0.00234 | 0.153 |
| 16 | 0.00195 | 0.130 |
| 24 | 0.00162 | 0.097 |

$12 \times 12$, $16 \times 16$, $24 \times 24$, and $48 \times 48$. At day 350 we computed the $L^2$ norm of the errors of the coarser grids as compared to our finest grid $48 \times 48$. The results are displayed in
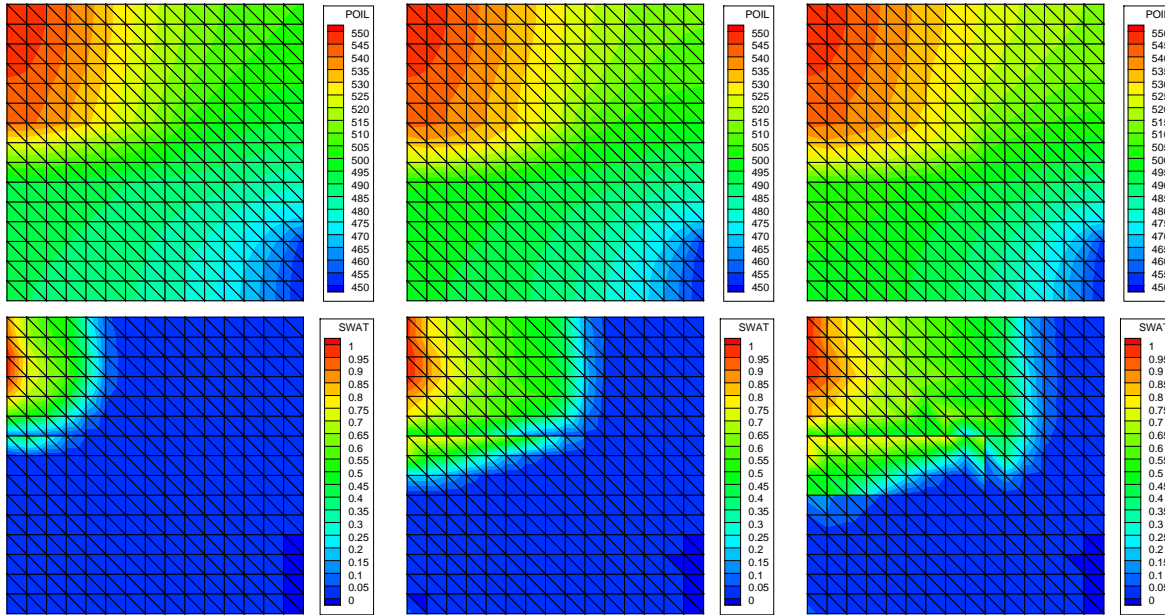
**Fig. 8** Primary pressure choice in 2-D. Oil pressure (top) and water saturation (bottom) with initial saturation 0 and using oil pressure as primary pressure. From left to right at day 300, 700, and 1000.
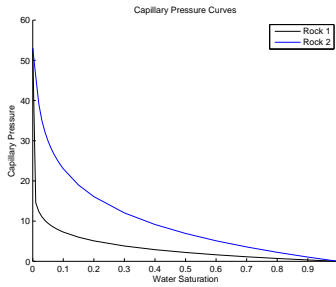


**Fig. 9** Capillary pressure curves for the mesh refinement study.

Table 1. We see reasonable convergence of the course solutions to the fine one. In fact, linear regression shows a convergence rate of about 0.68 for the pressure and 0.64 for the saturation.

## 5 Numerical examples in three dimensions

In the next series of tests, we use a cubical domain of size $(x, y, z) \in [0, 500] \times [0, 500] \times [0, 500]$ feet. Our tests include those with one and two rock types, and the effect of gravity is included in all tests.

For the single rock type examples, the initial water saturation is taken to be 0.2 and the pressure 500 psi (as in the two dimensional examples). These are actually set at the bottom of the domain, and distributed upward according to hydrostatic (i.e., gravity and capillary) equilibrium to the rest of the domain. For the two rock type examples, the initial water saturation is 0.3 in Rock 1 (at the bottom of the

reservoir), and Rock 2 is set to satisfy continuity of capillary pressure. Again the pressure is set to 500 psi at the bottom of the domain.
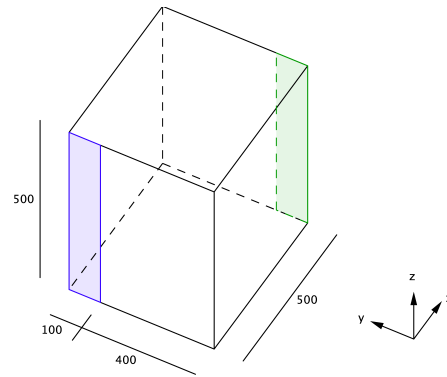


**Fig. 10** Three dimensional boundary conditions. No flow except on the blue inflow region and the green outflow region, where the pressure is specified.

We use a computational mesh of prisms. The domain is divided into a uniform grid of $10 \times 10 \times 10$ elements, and the tops of the elements are cross-hatched to form the triangular base of the prismatic elements. The system is driven by a vertical pressure boundary condition set to 550 psi at the bottom of the inflow face of $2 \times 10$ elements near a corner, and a vertical outflow face set to 450 psi at the bottom of $2 \times 10$ elements near the opposite corner (see Fig. 10). In some cases, we use a grid refined near the inflow region.

We will compare the use of the oil and water pressure variables as the primary variable in the pressure equation. It should be noted that the two problems are slightly different, given the way the boundary and initial conditions are set from the pressure, as noted in Section 4.3. In these three-dimensional examples, we use only the case of a linear approximation for both the primary pressure and the saturation.

All single rock type examples show results after 500 days of simulation. For these examples the porosity $\phi = 0.2$ and the permeability is $K = 100$ millidarcies for the single rock type examples, and $K$ is 100 for Rock Type 1 and 50 millidarcies for Rock Type 2 when there are two rock types. The single rock type examples have compressibility of water and oil set to $10^{-12}$ and $10^{-10}$, respectively, while for two rock types these are $10^{-7}$ and $10^{-5}$, respectively.

### 5.1 Brooks-Corey capillary pressure

The Brooks-Corey model is given by

$$p_c(S_w) = p_e S_w^{-1/\lambda}, \tag{29}$$

where $\lambda$ is the pore size index, typically and here taken as $\lambda = 2$, and $p_e$ is the entry pressure, which is proportional to $\sqrt{\phi/K}$, with the proportionality constant taken to be 100 (and so is $p_e = 4.47$ psi). We also test a dominant capillary pressure case which is 10 times stronger ($p_e = 44.7$ psi). The relative permeabilities are given by

$$k_w = S_w^{(2+3\lambda)/\lambda} \quad \text{and} \quad k_n = (1-S_w)^2(1-s_w^{(2+\lambda)/\lambda}). \tag{30}$$

On a technical note, the capillary pressure blows up as $S_w$ approaches 0, so we modified its asymptote to hit the $S_w = 0$ axis on a linear trajectory from $S_w = 0.01$. As used in our tests, these curves are shown in Figs. 11–12.
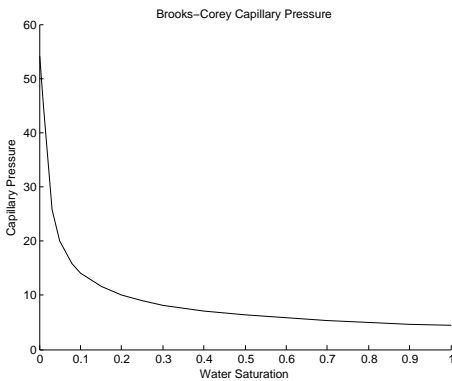


**Fig. 11** Brooks-Corey model. The capillary pressure (in psi).

Our results are shown in Fig. 13, using the oil pressure as the primary variable in the pressure equation, and
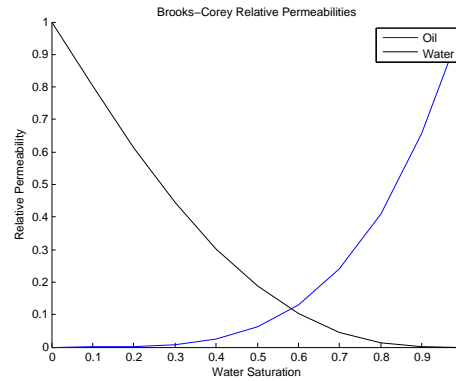


**Fig. 12** Brooks-Corey model. The relative permeabilities.

in Fig. 14, using the water pressure. As can be seen, the oil pressure gives a somewhat better result, since it is smoother and cleaner, as one should expect for an elliptic problem. We also show the same simulations using a grid refined near the inflow region in Figs. 15 and 16. There is little difference, indicating again that the method is accurate. Moreover, although refinement gives more accurate results, it is not strictly required for physically meaningful results. This is an important property in reservoir simulation, since computational power limitations dictate that the grid used is often coarser than one might like.

In the dominant capillary pressure case ($p_c$ is multiplied by 10), we again see a clean pressure in Fig. 17 for the primary oil pressure variable case. However, now we see a broader plume for the water saturation compared to the non dominant capillary case, as expected. For the case with the water pressure as the primary pressure, our code did not produce a physically reasonable solution.

### 5.2 Van Genuchten capillary pressure

The Van Genuchten model is given by

$$S_w = \left[1 + \left(\alpha p_c(S_w)\right)^n\right]^{-m}, \tag{31}$$

$$k_w(S_w) = \sqrt{S_w}\left[1 - (1 - S_w^n)^m\right]^2, \tag{32}$$

$$k_n(S_w) = (1-S_w)^2(1-S_w^n)^{2m}, \tag{33}$$

where $m = 1/n$ and we take $\alpha = 10/$psi and $n = 0.8$. The singularities were linearized at the ends from $S_w = 0.005$ and $S_w = 0.9995$. The linearization is not visible to the eye, and the curves are shown in Figs. 18–19. In this test, we have a singularity in the derivative of the capillary pressure at *both* ends of the saturation range ($S_w = 0$ or 1). We thus cannot say which phase pressure should be preferred as the primary pressure in the pressure equation. Nonetheless, we obtain better and more reliable results using the oil pressure.
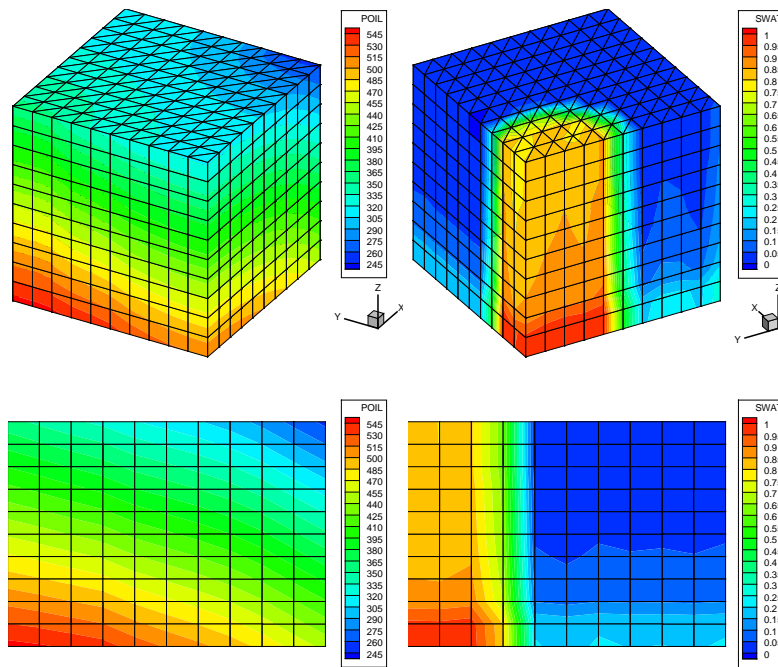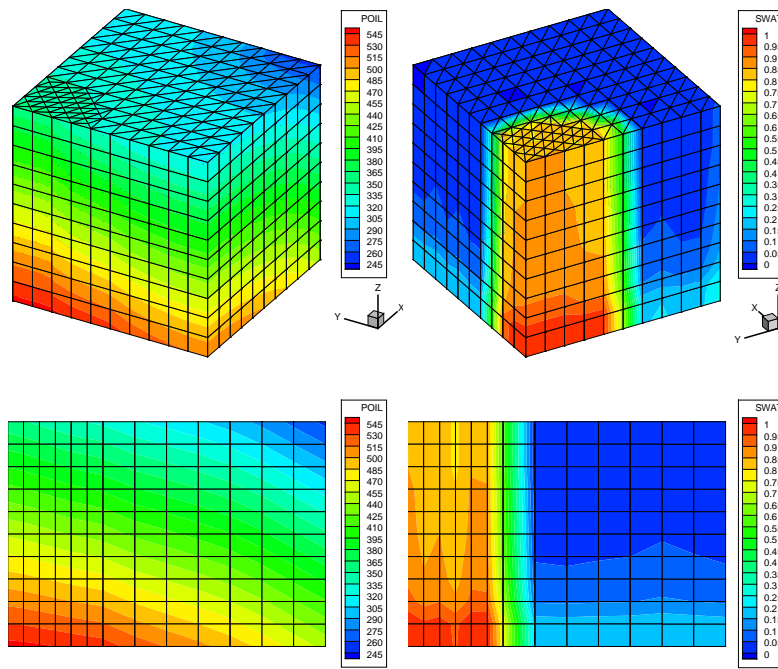
**Fig. 13** Brooks-Corey model. The primary variable is the oil pressure. On top is the full domain; on the bottom is a slice at 45 degrees between in and out flow. Linear oil pressure is on the left, and linear saturation is on the right.
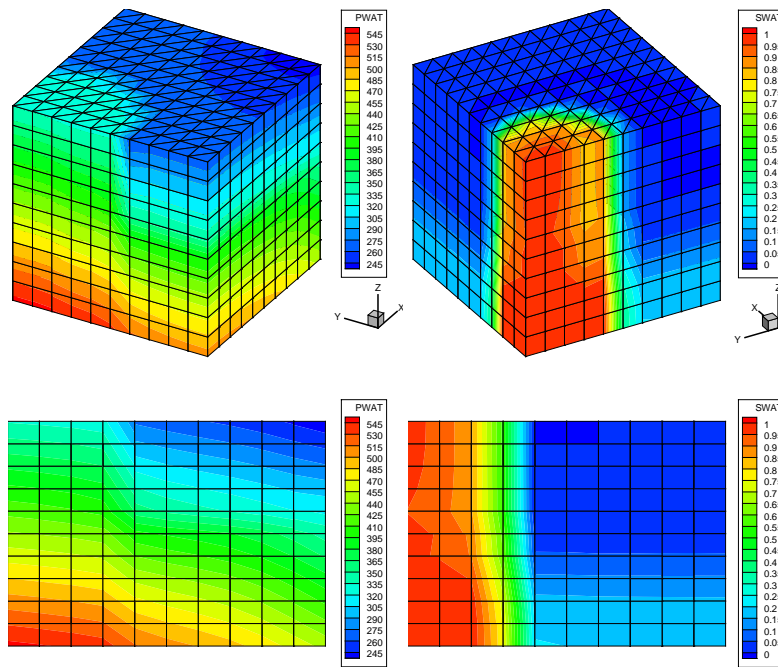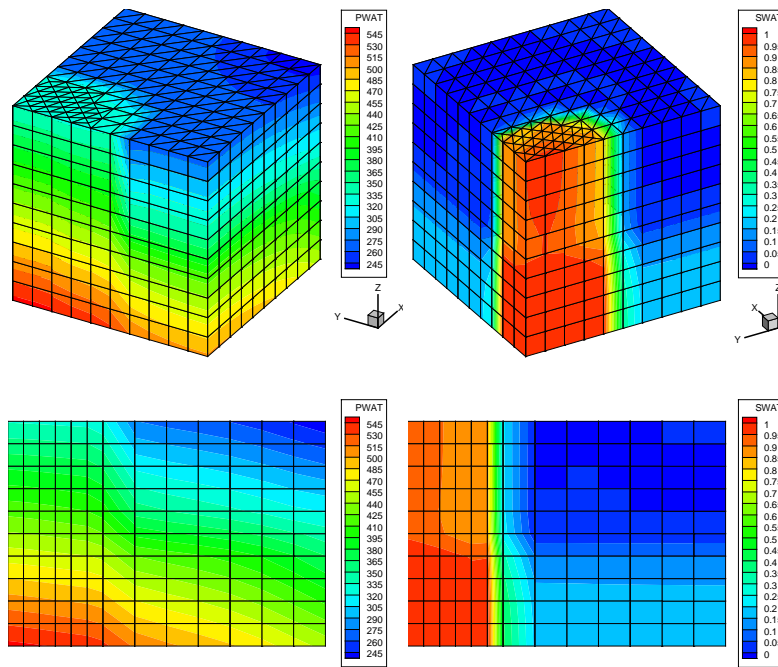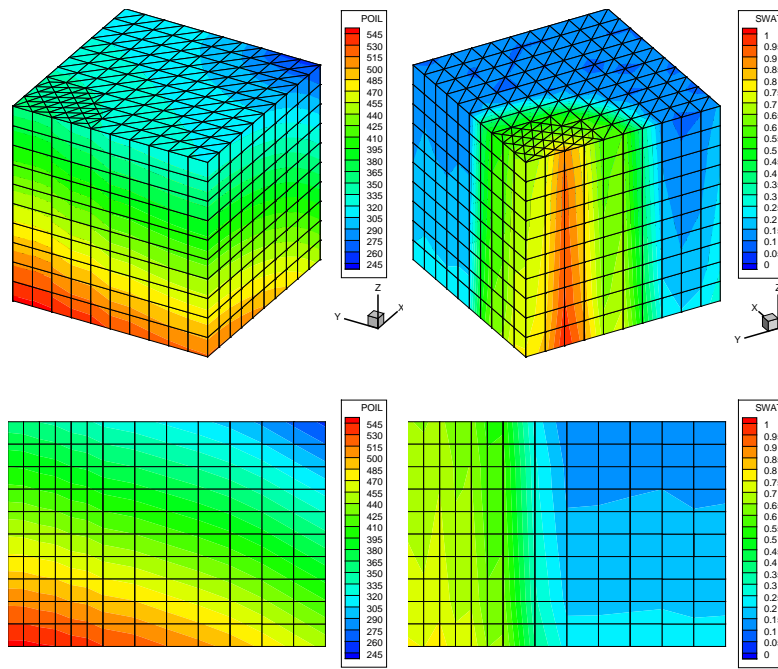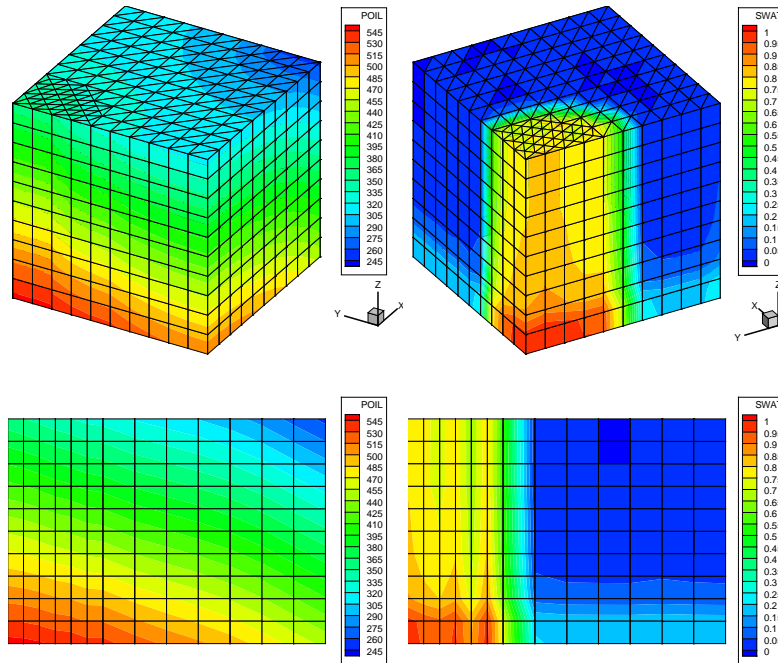


**Fig. 14** Brooks-Corey model. The primary variable is the water pressure. On top is the full domain; on the bottom is a slice at 45 degrees between in and out flow. Linear water pressure is on the left, and linear saturation is on the right.

**Fig. 15** Brooks-Corey model. The primary variable is the oil pressure, with a refined grid near inflow. On top is the full domain; on the bottom is a slice at 45 degrees between in and out flow. Linear oil pressure is on the left, and linear saturation is on the right.



**Fig. 16** Brooks-Corey model. The primary variable is the water pressure, with a refined grid near inflow. On top is the full domain; on the bottom is a slice at 45 degrees between in and out flow. Linear water pressure is on the left, and linear saturation is on the right.

**Fig. 17** Brooks-Corey model, capillary dominant. The capillary pressure is ten times greater than usual. The primary variable is the oil pressure, with a refined grid near inflow. On top is the full domain; on the bottom is a slice at 45 degrees between in and out flow. Linear oil pressure is on the left, and linear saturation is on the right.



**Fig. 20** Van Genuchten model. The primary variable is the oil pressure, with a refined grid near inflow. On top is the full domain; on the bottom is a slice at 45 degrees between in and out flow. Linear oil pressure is on the left, and linear saturation is on the right.
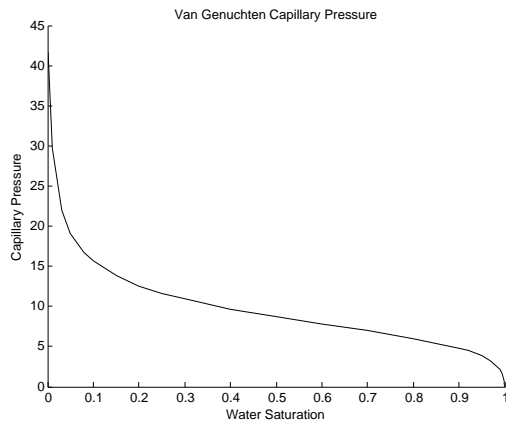
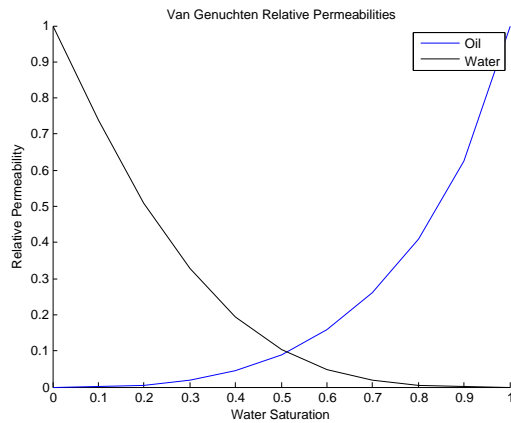**Fig. 18** Van Genuchten model. The capillary pressure (in psi).



**Fig. 19** Van Genuchten model. The relative permeabilities.

Our results on the refined grid are shown in Fig. 20, using the oil pressure as the primary variable in the pressure equation. The capillary dominated case (multiplying the capillary pressure by a factor of 10) is shown in Fig. 21. Reasonable results are obtained. When the water pressure was used as the primary pressure variable, the simulations did not run past 100 days for our code. We are not sure why, but perhaps this was due to the slightly different problem run. Due to the way the initial condition and boundary conditions are set, the water pressure problem is somewhat more difficult.

### 5.3 Two rock types in a layered configuration

The next two test cases concern domains with two rock types. In this first test, the rock types are arranged in a layered configuration. Rock Type 1 appears in the top and bottom four layers of elements, separated by Rock Type 2 in the center two layers of elements, as shown in Fig. 22.

The rock property curves for the two types of rock differ. For the Brooks-Corey model (29)–(30), both rocks use
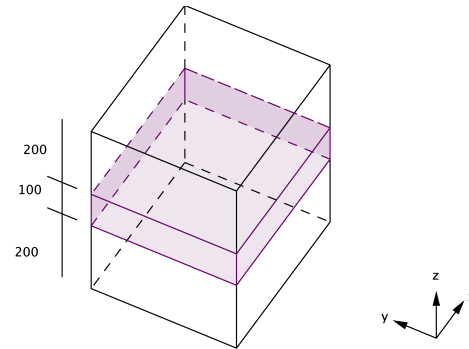


**Fig. 22** Two layered rock types. The center portion is Rock Type 2, which separates Rocks of Type 1.
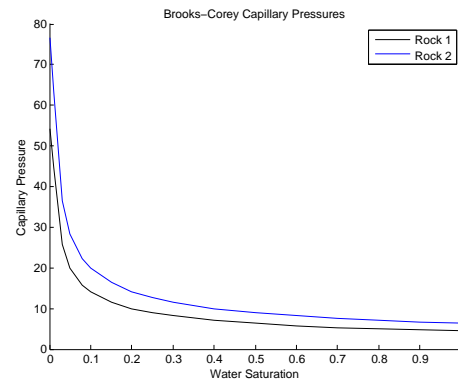


**Fig. 23** Two rock types. Capillary pressures for the Brooks-Corey model.

$\lambda = 2$ but they differ in the proportionality constant $p_e = 100\sqrt{\phi/K}$, which is $p_e^1 = p_e = 4.47$ for Rock Type 1, the same as for a single rock type, and $p_e^2 = 6.32$ for Rock Type 2. The capillary pressure curves are shown in Fig. 23.
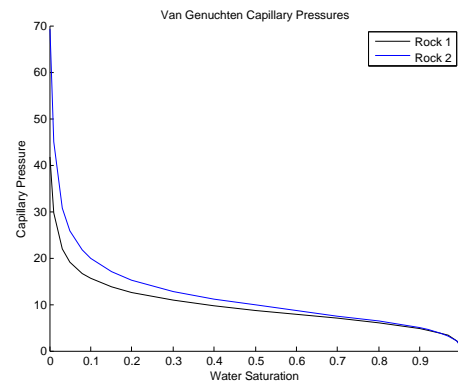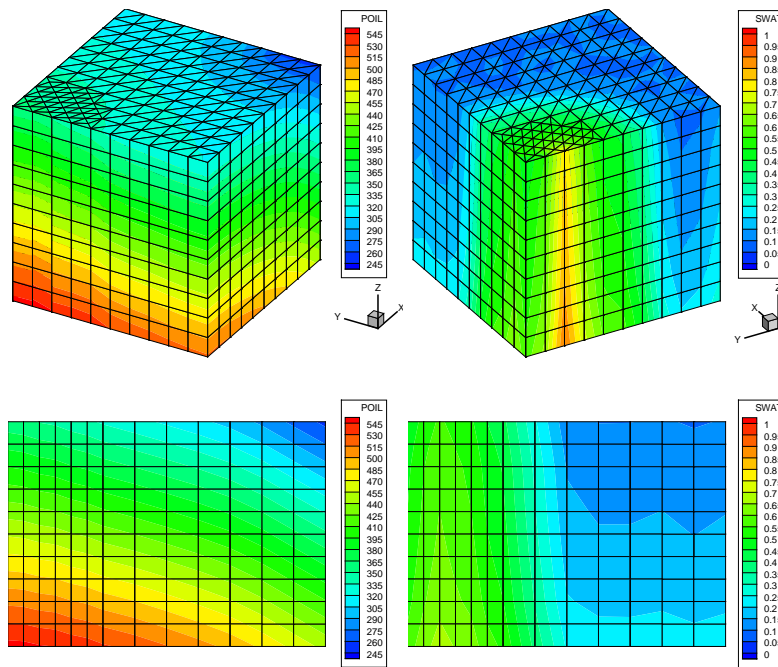


**Fig. 24** Two rock types. Capillary pressures for the Van Genuchten model.

For the Van Genuchten model (31)–(33), we use the same $n = 0.8$ for Rock Type 1 as for the single rock type exam-

**Fig. 21** Van Genuchten model, capillary dominant. The capillary pressure is ten times greater than usual. The primary variable is the oil pressure, with a refined grid near inflow. On top is the full domain; on the bottom is a slice at 45 degrees between in and out flow. Linear oil pressure is on the left, and linear saturation is on the right.
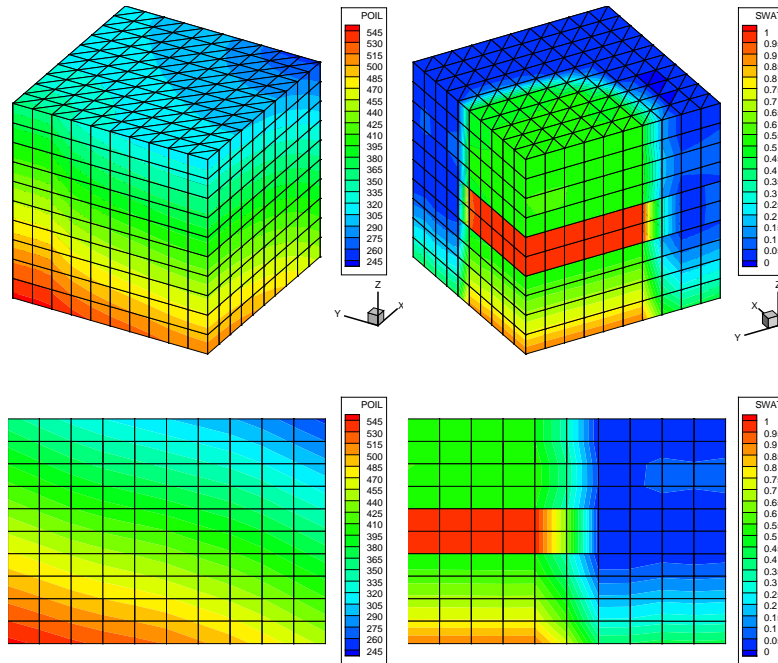


**Fig. 25** Two layered rocks of Brooks-Corey type. The primary variable is the oil pressure. On top is the full domain; on the bottom is a slice at 45 degrees between in and out flow. Linear pressure solutions on the left, and linear saturation solutions on the right.
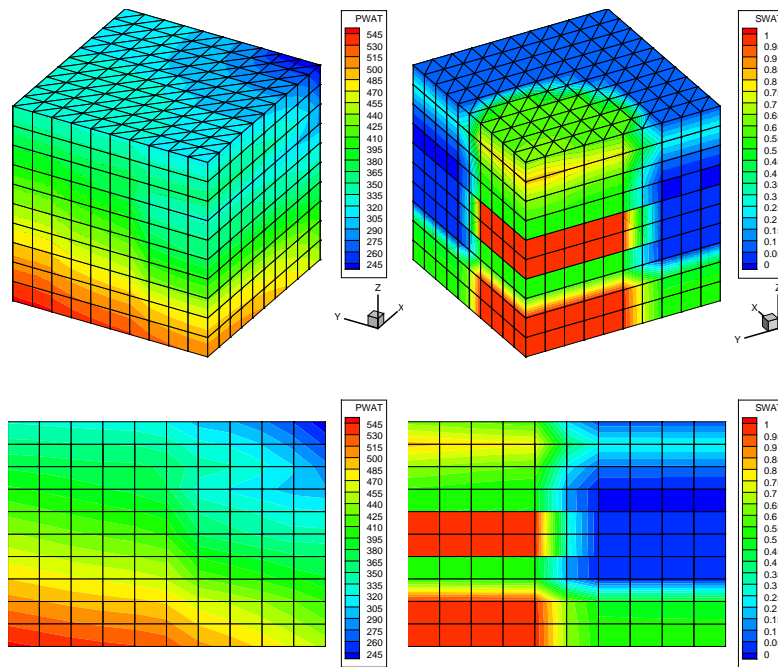
**Fig. 26** Two layered rocks of Brooks-Corey type. The primary variable is the water pressure. On top is the full domain; on the bottom is a slice at 45 degrees between in and out flow. Linear pressure solutions on the left, and linear saturation solutions on the right.
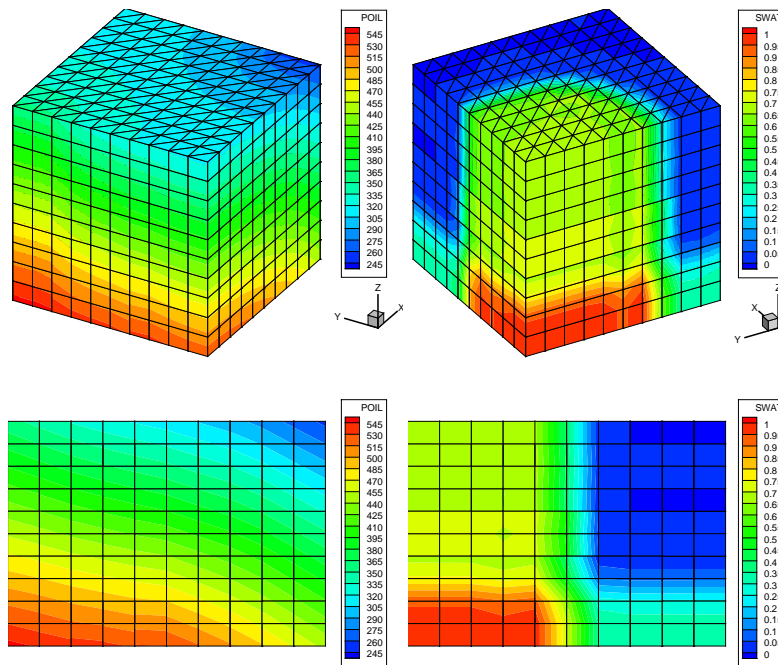


**Fig. 27** Two layered rocks of Van Genuchten type. The primary variable is the oil pressure. On top is the full domain; on the bottom is a slice at 45 degrees between in and out flow. Linear pressure solutions on the left, and linear saturation solutions on the right.

ples, and $n = 0.75$ for Rock Type 2. The capillary pressure curves are shown in Fig. 24.

We show results at 1200 days of simulation time. The Brooks-Corey results appear in Figs. 25–26, using the oil and water pressure as the primary variable, respectively. The very sharp, discontinuous change in saturation at the rock type interfaces is clearly evident, even as the pressure remains continuously varying. The case of the primary water pressure variable (Fig. 26) produces a physically unreasonable pool of water above the Rock Type 2 layer. This is perhaps due to the lack of a local slope limiter. The Van Genuchten results are in Fig. 27 (again, the use of the water pressure as primary variable led to nonconvergence before 100 days). The results appear very clean and reasonable.

### 5.4 Two rock types in a barrier configuration

Our final test has two rock types in a barrier configuration, as depicted in Fig. 28. This is the same configuration as the two dimensional example with two rock types, but now the model has vertical depth. The rock and fluid properties are the same as in the previous section (Section 5.3).
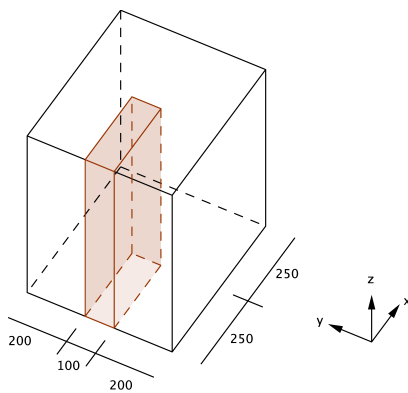


**Fig. 28** Two rocks in a barrier configuration.

In this example, we show results at 200, 700, and 1200 days of simulation time, so as to show the water plume before entering the barrier, while it is entering the barrier, and as it exits the barrier. The Brooks-Corey results appear in Figs. 29–30, using the oil and water pressure as the primary variable, respectively. The Van Genuchten results are in Fig. 31 (again, we did not see convergence for the water pressure as primary variable). As can be seen, the water moves ahead through the barrier due to the greater capillary pressure, producing a sharp discontinuity in the solution at the rock interfaces. The profile of saturation within the barrier at time 1200 days looks good in the slice, but not in the three dimensional rendering. This is again perhaps due to the lack of a local slope limiter. In essence, the saturation slopes the wrong way within the barrier (which is only two

elements thick). A good slope limiter should be able resolve this type of problem.

## 6 Conclusions and discussion

In this work we implemented two improvements to the discontinuous Galerkin formulation of the slightly compressible two phase flow solved using the IMPES scheme, which are projecting the velocity to the $H(\text{div})$ space and including an explicit penalty for the jump in the capillary pressure in the saturation equation. We showed that projecting the velocity to the $H(\text{div})$ space reduces the local oscillations. In some simple cases local oscillations are reduced to the point that one can use a a global slope limiter, which is much easier to implement and does not affect the dynamics of the solution as severely as a local limiter.

We showed that adding the penalty for the jump in the capillary pressure improved the saturation step considerably. With this formulation we observed that the saturation always fulfilled the continuity of the capillary pressure even if the magnitude of the capillary pressure was small compared to the phase pressures.

We also showed that choosing the non-wetting phase pressure as the primary pressure is often more numerically stable. This is to be expected for a Brooks-Corey type capillary pressure function, where the capillary pressure function has a steep gradient near the wetting phase residual saturation, but not at the oil residual saturation. It is perhaps somewhat surprising that we found in our test cases, the oil pressure was also preferred for Van Genuchten curves, which have singular capillary behavior at both residual saturations. Further study of this phenomenon is warranted, since we do not believe that our test suite is rich enough for a definitive conclusion for Van Genuchten type curves.

Research on coupled DG-DG methods for two-phase flow is far from complete. We have shown improvements, but much work remains. Our three dimensional results showed that an effective local slope limiter is needed to avoid nonmonotonic behavior. Our code does not include a proper well model, and this hampered our efforts to simulate appropriate test cases. The solver technology needs to be improved to speed up the wall clock time. We were forced to use a very small time-step, which suggests that a better, perhaps more implicit, coupling between the pressure and saturation equations is needed.

## References

1. T. Arbogast, G. Pencheva, M. F. Wheeler, and I. Yotov. A multiscale mortar mixed finite element method. *Multiscale Model. Simul.*, 6(1):319–346 (electronic), 2007.

2. P. Bastian and B. Rivière. Superconvergence and H(div) projection for discontinuous Galerkin methods. *Int J Numer Meth Fl*, 42:1043–1057, 2003.

3. J. Bear and A. H.-D. Cheng. *Modeling Groundwater Flow and Contaminant Transport*. Springer, New York, 2010.

4. F. Brezzi and M. Fortin. *Mixed and hybrid finite element methods*, volume 15 of *Springer Series in Computational Mathematics*. Springer-Verlag, New York, 1991.

5. Z. Chen, G. Huan, and Y. Ma. *Computational methods for multiphase flows in porous media*. Computational Science & Engineering. Society for Industrial and Applied Mathematics (SIAM), Philadelphia, PA, 2006.

6. H. Class, A. Ebigbo, R. Helmig, H. Dahle, J. Nordbotten, M. Celia, P. Audigane, M. Darcis, J. Ennis-King, Y. Fan, B. Flemisch, S. Gasda, M. Jin, S. Krug, D. Labregere, A. Naderi Beni, R. Pawar, A. Sbai, S. Thomas, L. Trenty, and L. Wei. A benchmark study on problems related to co2 storage in geologic formations. *Computational Geosciences*, 13(4):409–434, 2009.

7. C. N. Dawson, S. Sun, and M. F. Wheeler. Compatible algorithms for coupled flow and transport. *Comput. Methods Appl. Mech. Engrg.*, 193(23-26):2565–2580, 2004.

8. Y. Epshteyn and B. Rivière. Fully implicit discontinuous finite element methods for two-phase flow. *Appl. Numer. Math.*, 57(4):383–401, 2007.

9. A. Ern, I. Mozolevski, and L. Schuh. Discontinuous galerkin approximation of two-phase flows in heterogeneous porous media with discontinuous capillary pressures. *Comput. Methods Appl. Mech. Engrg.*, 199(23-24):1491 – 1501, 2010.

10. A. Ern, I. Mozolevski, and L. Schuh. Accurate velocity reconstruction for Discontinuous Galerkin approximations of two-phase porous media flows. *C. R. Acad. Sci. Paris*, 347(9-10):551–554, 2009.

11. A. Ern, S. Nicaise and M. Vohralík. An accurate flux reconstruction for discontinuous Galerkin approximations of elliptic problems. *C. R. Acad. Sci. Paris*, 345(12):709–712, 2007.

12. H. Hoteit and A. Firoozabadi. Numerical modeling of two-phase flow in heterogeneous permeable media with different capillarity pressures. *Advances in Water Resources*, 31(1):56–73, 2008.

13. D. W. Peaceman. *Fundamentals of numerical reservoir simulation*. Elsevier Scientific Pub. Co., Amsterdam, 1977.

14. S. Sun and M. F. Wheeler. Symmetric and nonsymmetric discontinuous Galerkin methods for reactive transport in porous media. *SIAM J. Numer. Anal.*, 43(1):195–219, 2005.

15. S. Sun and M. F. Wheeler. Projections of velocity data for the compatibility with transport. *Comput. Methods Appl. Mech. Engrg.*, 195(7-8):653–673, 2006.

16. The University of Texas at Austin. Center for Subsurface Modeling. `http://csm.ices.utexas.edu/`.

17. M. Wheeler, G. Xue, and I. Yotov. A multipoint flux mixed finite element method on distorted quadrilaterals and hexahedra. *Numerische Mathematik*, 121(1):165–204, 2012.

18. X. Zhang and C.-W. Shu. On maximum-principle-satisfying high order schemes for scalar conservation laws. *Journal of Computational Physics*, 229(9):3091 – 3120, 2010.
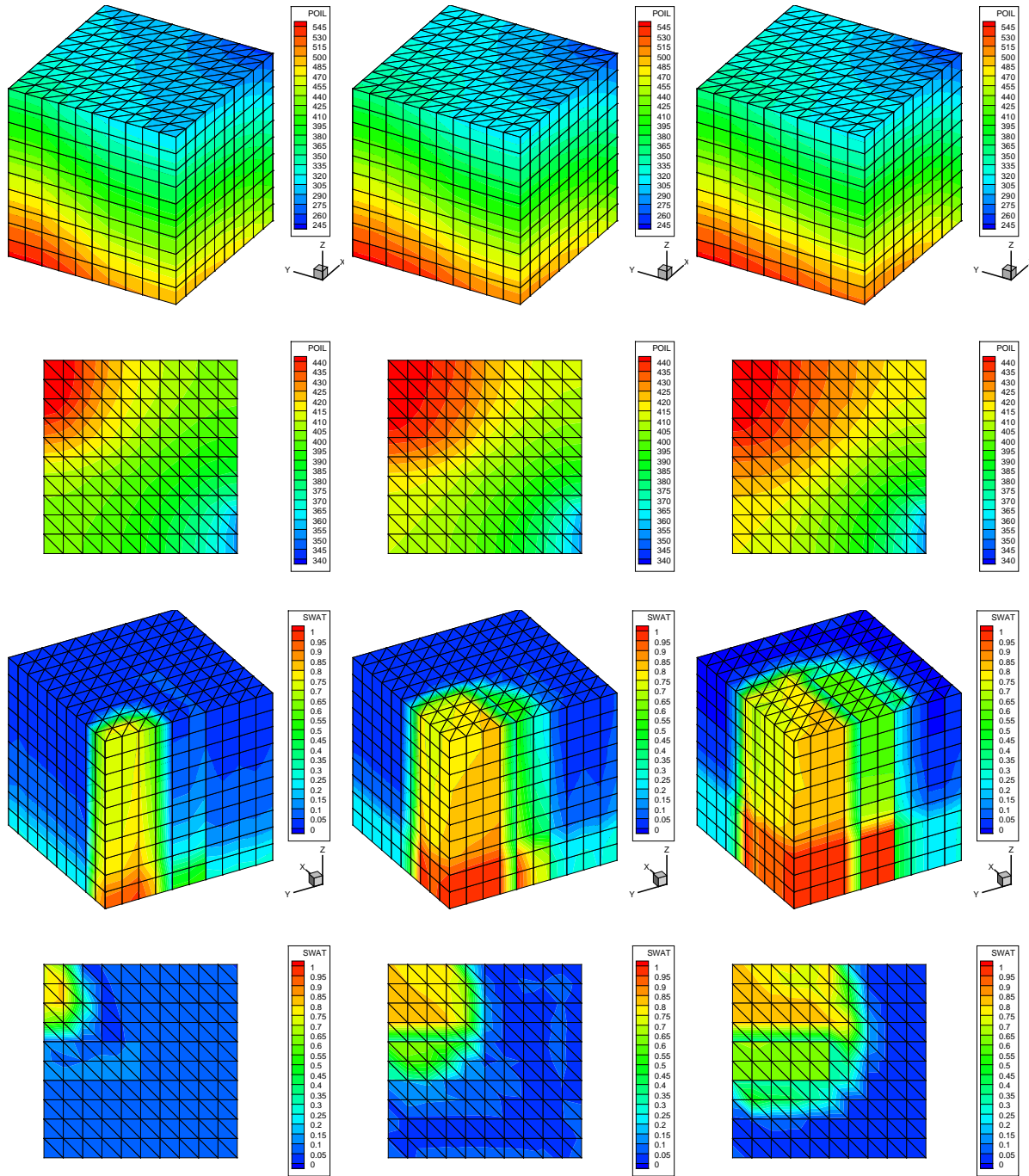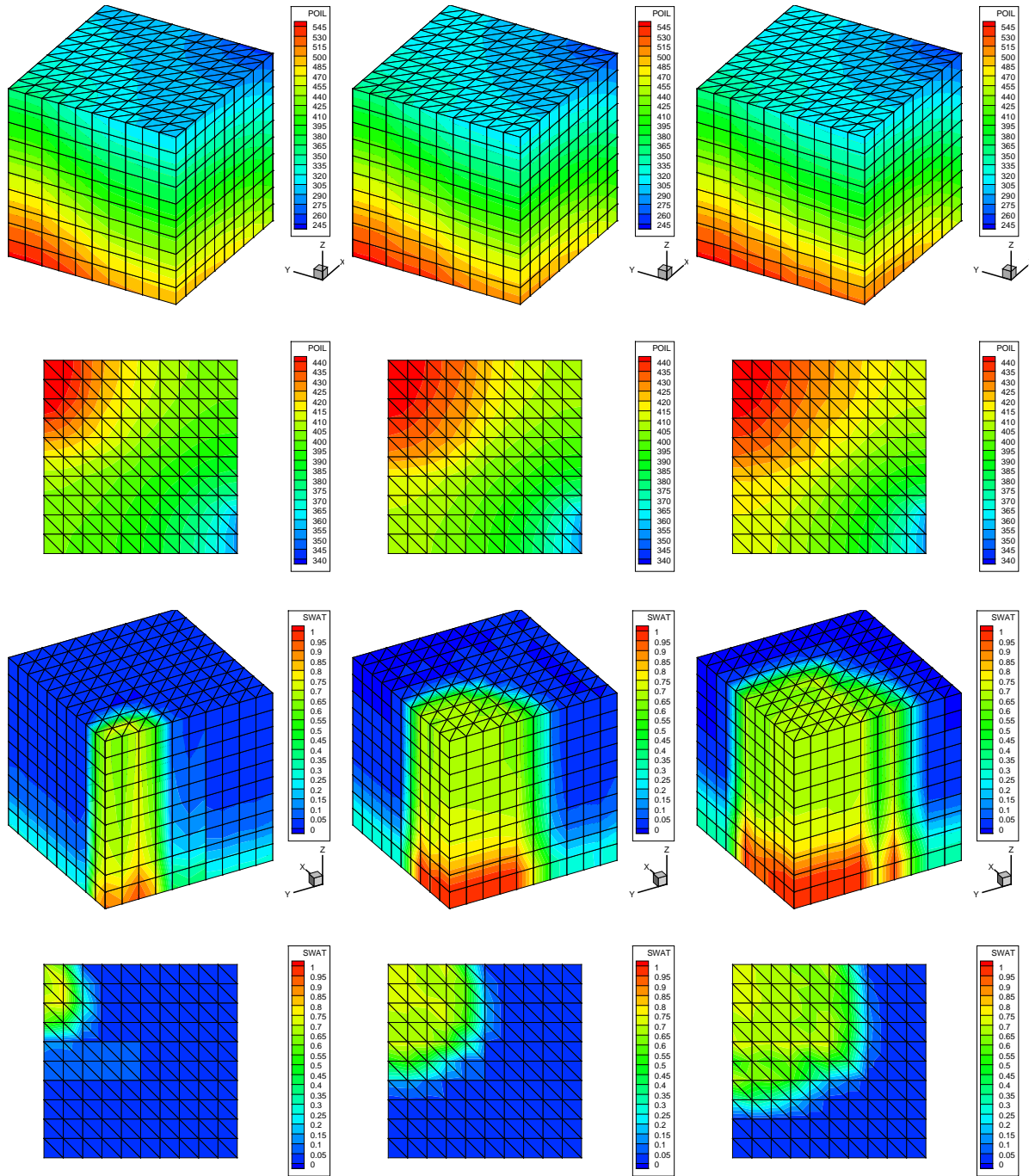
**Fig. 29** Two rocks in a barrier configuration and of Brooks-Corey type. The primary variable is the oil pressure. From left to right is the solution at 200, 700, and 1200 days, respectively. The top two rows are the linear pressure solution, with the slice at the middle of the domain in the z-direction (using a different color scale). The bottom two rows are the linear saturation solution, with the slice at the same location.
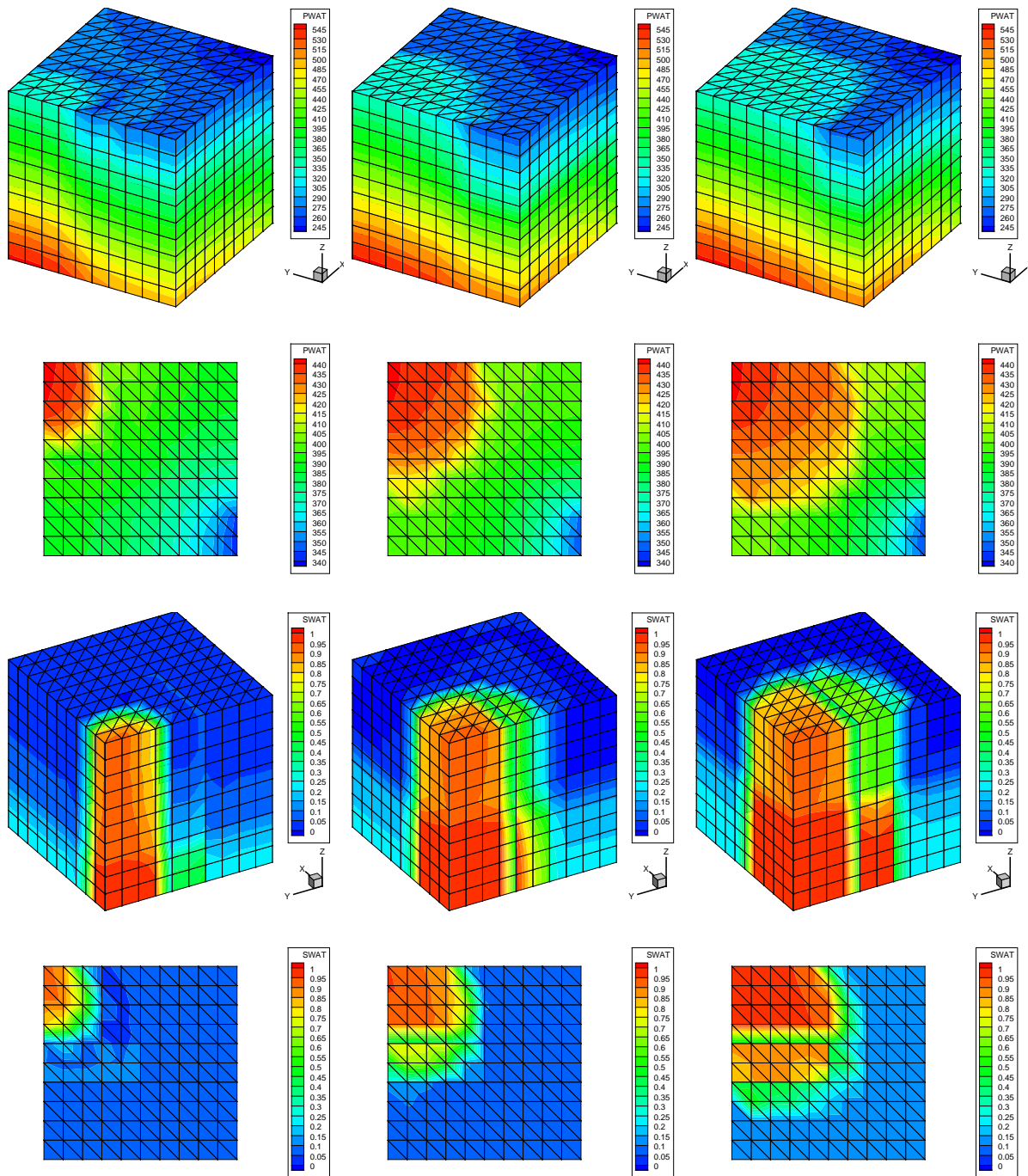
**Fig. 30** Two rocks in a barrier configuration and of Brooks-Corey type. The primary variable is the water pressure. From left to right is the solution at 200, 700, and 1200 days, respectively. The top two rows are the linear pressure solution, with the slice at the middle of the domain in the z-direction (using a different color scale). The bottom two rows are the linear saturation solution, with the slice at the same location.

**Fig. 31** Two rocks in a barrier configuration and of Van Genuchten type. The primary variable is the oil pressure. From left to right is the solution at 200, 700, and 1200 days, respectively. The top two rows are the linear pressure solution, with the slice at the middle of the domain in the z-direction (using a different color scale). The bottom two rows are the linear saturation solution, with the slice at the same location.